To be published as a Chapter in CRC Handbook of Nuclear Medicine Section on "Physics and Instrumentation," Richard P. Spencer, ed., CRC Press

LBL-4897

SEMICONDUCTOR DETECTORS IN NUCLEAR MEDICINE IMAGING

Jorge Llacer

June 1976

Prepared for the U. S. Energy Research and Development Administration under Contract W-7405-ENG-48

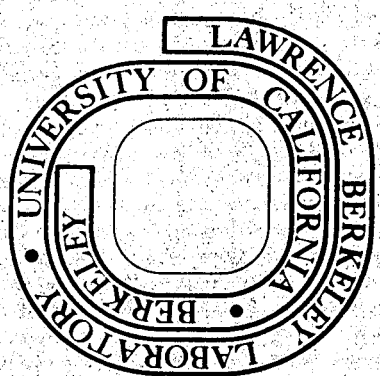

DISCLAIMER

LBL-4897

CRC Handbook of Nuclear Medicine
Section on "Physics and Instrumentation"

SEMICONDUCTOR DETECTORS IN NUCLEAR MEDICINE IMAGING*

Jorge Llacer, Ph.D.

Lawrence Berkeley Laboratory
University of California
Berkeley, California 94720 U.S.A.

Semiconductor radiation detectors are beginning to find a useful place in nuclear medicine imaging by virtue of their excellent energy resolution, which may generally be quoted as being in the neighborhood of 1% full width at half maximum (FWHM) for clinically useful detector configurations. In contrast, the more conventional NaI(Tl) photomultiplier systems exhibit resolutions ranging between 10 and 25% FWHM depending primarily on energy. The importance of energy resolution in imaging stems from: a) the relative need to prevent X- or γ-rays scattered by tissue surrounding a source from contributing to the image formation process, and b) from the need to separate an energy peak from spectral background or from other energy peaks in the spectrum of the source to be imaged.

Scattered radiation reduces contrast and is undesirable in general; therefore, the discrimination afforded by better energy resolution can be useful. However, in the field of radio-nuclide imaging, semiconductor detector systems of sufficient size to compete in efficiency with NaI systems have either not been made or not tested well in a clinical environment as yet. An unequivocal answer to the question of the importance of improved scatter rejection in nuclear medicine diagnosis does not exist either, although preliminary tests and a

---

* This report was done with support from the United States Energy Research and Development Administration. Any conclusions or opinions expressed in this report represent solely those of the author and not necessarily those of The Regents of the University of California, the Lawrence Berkeley Laboratory or the United States Energy Research and Development Administration.

substantial amount of theoretical work indicate that definite improvements of imaging will result in specific practical situations from the use of semiconductor detector scanners and cameras.

Semiconductor detectors have already proven very successful in another area of nuclear medicine imaging, that of fluorescent scanning of shallow organs. Imaging of the thyroid by this method is becoming an established technique.

This article briefly discusses the present state of theoretical and experimental work on radio-nuclide imaging and of fluorescent scanning using semiconductor detectors, supplying sufficient references for the interested reader to obtain more detailed information from the literature. Good introductions to the principles of operation of lithium-drifted silicon and germanium detectors and the associated electronics have been given by Goulding and Stone[1], Armantrout[2], and Bradley[3]. High-purity germanium detectors, which are essential for fabricating stable germanium detector arrays, are described by Baertsch and Hall[4], Llacer[5,6], Pehl, Cordi and Goulding[7], Hansen and Haller[8], and by Marler and Hewka[9]. In a recent development, Hall and Soltys[10] have introduced a radial gradient of impurities on high-purity germanium crystals which may simplify the fabrication of very large-volume detectors, in the region of 80 cm^3, made from crystals of greater than 4.5 cm diameter.

I. RADIOISOTOPE IMAGING

A. Theoretical Work

Beck, et al[11] have shown the theoretical advantages of eliminating scattered radiation in imaging systems. Two principal criteria are developed, 1) that of Modulation Transfer Function (MTF), which is a measure of the ability of a system to transfer information from a source to an observer in terms of spatial frequencies and 2) a figure of merit which takes into consideration the MTF of a system and the sensitivity (efficiency) of the detector. Marking suitable approximations on the nature of the scattered radiation, Beck et al show how the MTF of a NaI imaging system suffers substantial degradation when a line source is embedded in an absorber, while that of a Ge detector suffers negligible degradation. On the other hand, the figure of merit for the Ge detector system used in a scanner for the reported work was worse than that of a NaI system due to the relative small size of the Ge(Li) detector available at the time.

The concept of the figure of merit for the comparison between NaI and Ge as detectors for gamma-ray imaging has been further expanded by Strauss and Sherman.[12] They have developed an imaging merit factor based only on the fundamental characteristics of energy resolution and photopeak detector efficiency of both materials. Their merit factor increases with the increased energy resolution of Ge because 'noise' due to scattering in the absorber surrounding the source is effectively eliminated from the image. On the other hand, it is decreased in Ge by the fact that its lower photoelectric cross section for gamma-rays results in higher scattering within the detector. In a scanner this second factor does not affect the determination of the coordinates of the point from which the gamma-rays are emitted, but in a Ge camera with small independent picture elements, scattered events in the detector produce false positional information unless they are rejected by the electronic circuits. Strauss and Sherman conclude that, based only on the two fundamental detector materials parameters indicated, their merit factor for Ge scanners can be better than that of NaI systems. All that is required is sufficient detector area and volume.

For the case of cameras, their merit factor for Ge is 10 to 18% lower than for NaI, except when the camera circuits reject events which occur in more than one picture element, in which case the materials are very similar. The fact that the coordinates of a photoelectric event in NaI Anger-type cameras cannot be determined exactly due to light scattering has not been considered by Strauss and Sherman, with the result that their figure of merit for Ge cameras in comparison with NaI is lower than it might be.

A different and, in part, complementary approach to the evaluation of the benefits to be obtained by Ge imaging was followed first by Kraner, Llacer and Atkins[13], and then by Llacer[14] and Llacer and Graham[15]. In all cases MTF analysis of the effects of removing scattering by the utilization of Ge detectors has been carried out from the line response functions of actual systems. Changes of phantom image (real or computer generated) corresponding to changes in MTF due to scattering rejection have been shown. Parameters such as count rates and imaging time have been taken into consideration. As a result, a fairly clear picture of where Ge detectors can be most important has emerged. The conclusions arrived at seem to be substantiated by the small amount of clinical work existent to date, as will be described below.

Kraner, et al[13] succeeded in developing a Ge(Li) detector of large area which had a photopeak efficiency of 50% compared to a 7.6 x 5.1 cm (3" x 2") NaI crystal. Energy resolution was 4.6 KeV FWHM at 140 KeV. With this detector the authors were able to verify the almost complete insensitivity of the Ge system MTF to the presence of 7 cm of lucite absorber, while the NaI detector MTF showed substantial degradation, well in agreement with the results of Beck, et al[11]. Comparative scans of a phantom filled with ^{99m}Tc with the NaI and Ge detector heads in the presence of a 7 cm absorber at equal scanning speeds and equal scanning times showed very little difference in the images of hot spots of different sizes. Substantially better imaging of cool spots with the Ge detector was observed, however, in spite of the poorer statistics obtained with that detector (efficiency 50%). Figure 1 shows the results of this direct comparison.

In the study of Ref. 14, based on the performance of Ge detector scanners with ^{99m}Tc and high contrast sources (bar patterns) embedded in the absorber, Llacer arrives at the conclusion that detector energy resolution becomes increasingly important when collimators of finer spatial resolution are used. For the 1045 hole, 3.4 cm thick Pb collimator also used by Kraner, et al,[13] bar patterns which would be imaged clearly with detectors of perfect energy resolution (0 KeV FWHM) appear just as clear with a detector of 8 KeV FWHM. On the other hand, for a collimator with four times narrower line response function, a 4 KeV FWHM detector is reducing contrast quite substantially, when compared to a perfect detector.

In Ref. 15, Llacer and Graham concentrated primarily on the performance of cameras and low contrast cources. By obtaining MTFs from two commercial cameras and from a one-element Ge camera and using these results in a computer simulation of images, they show that the imaging of cool spots of 70% activity and 1 cm or 0.5 cm diameter in circular fields of 9 cm diameter and 100% activity may benefit from the superior energy resolution of Ge. To obtain that benefit, however, sharper collimators than the ones currently used in clinical practice would be needed. The relationships between collimator parameters and size of detectable cool spots is examined in the paper. Figure 2 shows the effect of detector energy resolution on the computer generated image for the two cool spots indicated above, as they would be obtained by a camera equipped with a collimator of approximately 1/3 the transmission of the high resolution collimator made for

^{99}Tc by Nuclear Chicago for their H-P camera. The images with a window W = $\pm$ 2.4 KeV correspond to those of a Ge detector system, W = $\pm$ 14 KeV correspond approximately to those of a 20% window in a well coupled NaI-photomultiplier combination, showing little degradation, while the images for W = $\pm$ 35 KeV, corresponding to a NaI camera coupled with a complex light pipe system, show considerable degradation. Since Ge cameras can be made with the higher intrinsic resolution (small element size) needed to utilize profitably collimators which are sharper than the ones now currently in use, one can conclude from the above study that Ge cameras (as well as scanners) have their principal strength in extending the range of imaging to difficult low contrast small objects. The increase in imaging time needed for this extension is, however, quite painful--not only are finer collimators slower, but there is a basic requirement of better statistics for detection of smaller objects. Refs. 14 and 15 make a quantitative assesment of these requirements.

It must be pointed out that theoretical studies are based on flat (two-dimensional) sources. In many real clinical situations with three-dimensional sources one can expect that the benefits of high-energy resolution will be more important than indicated by theoretical studies, as was already recognized by Beck in 1971 (Ref. 11, discussion). One can expect, therefore, better imaging with Ge, even with standard collimators, if sufficient time is allowed with small detector systems, or systems with larger detectors are fabricated.

B. Experimental and Clinical Work

1. Ge scanners:

Three principal research groups have been particularly active in the evaluation and use of Ge scanners: at the Franklin McLean Memorial Research Institute, University of Chicago, at Hammersmith Hospital, in London, and at Vanderbilt University, Nashville, Tennessee. Hoffer and Beck[16] (Franklin McLean) have shown improved diagnosis capabilities from brain scans with ^{99m}Tc. The Ge(Li) detector used was of quite small dimensions (14 cm^2 area) and, therefore, not generally useful for clinical use. Figure 3 shows the right lateral brain scan view of a patient scanned with a conventional NaI (Tl) detector scanner and with a Ge(Li) detector.

Collimators and light projectors were comparable. The patient had symptoms of cerebral metastasis from a known carcinoma of the breast. On the basis of the NaI scan, a solitary brain metastasis was thought to exist and surgery was contemplated. The Ge scan revealed a second metastasis in the right motor strip region, and the surgical procedure was cancelled.

Figure 4 shows a left lateral view in a patient with a suspected brain tumor. On the basis of the NaI scan, a lesion was described in the left posterior temporal region. (The choroid plexus was blocked with a 1 gm perchlorate before scanning.) The Ge scan revealed that the apparent 'mass' in the left temporal region had a linear configuration and joined the left lateral sinus. It was then decided that the 'lesion' in the left temporal lesion was in fact a superficial draining sinus. This diagnosis was confirmed by arteriography.

Hoffer and Beck report that the Ge detector failed to provide improved imaging of a liver lesion and they prove that this is clearly due to the effect of respiratory motion. This result brings up the possible advantage of a Ge camera over a scanner, as the former can be gated to any approximately periodic motion of the body and the improved imaging capability of Ge detectors can be exploited better.

Kirby, et al[17] have recently completed a set of three Ge(Li) detectors mounted in a single cryostat providing a detector surface of 83 cm^2, a volume of 249 cm^3, a photopeak efficiency of 93% that of a 7.6 x 7.6 cm (3" x 3") NaI detector at 122 KeV, and an energy resolution of 3.2 KeV FWHM. This detector is to be used for efficient scanning in a clinical environment at the University of Chicago and to test the theory of optimum utilization of all detected radiation by Beck, et al[18].

Glass, et al[19] (Hammersmith) report the use of a planar Ge(Li) detector with 70 mm diameter and 15 mm thickness with a photopeak efficiency of 40% with respect to a 7.6 x 5.1 cm (3" x 2") NaI

detector. In spite of the low efficiency of the detector system, they report improved diagnosis capabilities with Ge scans of the brain. It appears that their results bear out clinically the results obtained by Kraner, et al[13] from phantom studies. Even with the poorer statistics in the images of a Ge detector with 40% or 50% relative efficiency, the scans obtained provide more information than those obtained with the corresponding 100% efficient NaI detector system. This result is also in agreement with the theoretical results of Strauss and Sherman[12] which show a higher fundamental imaging efficiency for Ge scanners than for NaI scanners.

The philosophy of the group at Vanderbilt University has been quite different. Since they have had available to them only two quite small Ge detectors with low figures of merit, but excellent energy resolution, they have used them in applications for which their small size was not an important factor. Brill, et al[20] reports the simultaneous administration of multiple radioactive tracers to animals with spontaneous tumors and have used Ge detectors in a scanner configuration, separating the different images of different isotopes by simultaneous use of independent energy windows. The time saving and the quality of the comparative data obtained by this procedure are found to be very valuable in placing tracers in proper perspective. They have also used Ge detectors in fluorescent scanning of high atomic number tracers, as will be discussed later.

The group at Vanderbilt University has recently been supplied (by the Lawrence Berkeley Laboratory, U.C. Berkeley) with an array of nine high-purity Ge detectors, each of 35 mm diameter and 10 mm thickness, arranged in a 3 x 3 configuration with 50 mm between centers. The energy resolution of each detector is 1.1 KeV FWHM at 140 KeV. The photopeak efficiency of the system at 140 KeV is approximately 41% with respect to a 12.7 x 12.7 cm (5" x 5") NaI crystal. The system is expected, therefore, to be adequate to study the capabilities of a Ge scanning system in a routine clinical environment.

2. Germanium cameras:

Work on multielement Ge cameras has been carried out principally by four groups: 1) at the Institute of Cancer Research, Sutton, Survey and the U. K. Atomic Energy Authority, U. K., 2) at the Sloan-Kettering Institute of Cancer Research, New York, 3) at the University of California Medical School, San Francisco and the Lawrence Livermore Laboratory, California, and 4) at the Ohio State University, Columbus, Ohio. In addition, the feasability of making a camera using a coaxial Ge(Li) detector has been demonstrated at the Argonne National Laboratory, Argonne, Illinois.

Parker, et al have made an assessment of their results with orthogonal strip Ge(Li) cameras from their initial work in 1968 to 1972.[21] The main emphasis of their work has been given to understanding the advantages and disadvantages of a Ge camera when compared to an Anger type camera. Their more recent work is based on a 15 x 15 cell camera made from a single slice of lithium drifted germanium. Cell centers were 3 mm apart, with a cell area of 3.6 mm^2 (1.9 x 1.9 mm) and a sensitive depth of 6.5 mm. The photopeak efficiency at 140 KeV for one of the cells was found to be 25%, which is approximately 1/3 that of an Anger camera. The Ge camera in a high resolution configuration was fitted with a collimator which transmitted approximately 1/3 the number of counts of a high resolution collimator for the Anger camera used for comparisons. The reduction in transmission was mostly due to increased sharpness by using smaller, longer holes, but also by using thicker septa to reduce penetration. The resultant camera was approximately ten times slower than a portion of an Anger camera of the same size. The Ge(Li) detector proved to be somewhat unstable with time, but allowed those workers to arrive at the conclusion that Ge cameras would provide main clinical gains when deep lying organs are studied -- particularly when attempting to obtain accurately the shape of inactive regions. These conclusions are very much in agreement with the theoretical work of Llacer and Graham[15] for Ge cameras.

Detko[22] at the Sloan-Kettering Cancer Center has placed most of the emphasis in his work on obtaining stable elements for a Ge camera. His most recent work is with high-purity germanium, eliminating the uncertainties of the Li-drifting process. In studies of detector element efficiency stability over periods of more than one year, of effects of temperature cycling and of exposure of an array to air, voluntarily or accidentally, Detko has come to the conclusion that the fabrication of Ge camera orthogonal strip elements requires surface passivation techniques if the detector is to be reliable under the above conditions. In the fabrication of a large camera by putting together a number of Ge elements with orthogonal strips, it is necessary that exposure to ambient air over long periods of time does not change detector leakage current and photopeak efficiency by changes in detector surface conditions. Detko reports the successful passivation of 10 x 10 cell detector elements, with an inter-cell distance of 3 mm, a cell area of approximately 6.25 mm^2 (2.5 x 2.5 mm) and an active depth of 9 mm. Photopeak cell efficiency is reported to be approximately 58% for the 122 KeV and 135 KeV gamma-rays of ^{57}Co. The passivated element has withstood outrageous tests, including exposure to air while cooled to liquid nitrogen temperature, without suffering degradation in any of its important characteristics.

Kaufman, et al[23] at the University of California Medical School in San Francisco and at the Lawrence Livermore Laboratory have developed the prototype element for a future large high-purity Ge camera and have proceeded to obtain a number of animal images with different isotopes and collimators in order to learn its strong and weak points. The detector element is made in a configuration of 10 x 10 cells, occupying 2 x 2 cm^2, with inter-cell spacing of 2 mm and a thickness of 8 mm. Energy resolution at 140 KeV is 4.8 KeV FWHM and a delay line readout is used to determine the coordinates of the interaction. Although the individual detector cells are quite small in cross section and the photopeak efficiency of a cell in response to a point source should be of the order of 35%, the authors report an efficiency of 50% for their cells. This increase

in efficiency can be explained by noting that in a delay line read-out system gamma-ray interactions which occur in more than one element by Compton scattering add their energies and are, therefore, accepted. The resulting positional information for such events is given by a signal which is inherently 'noisy', as defined by Strauss and Sherman,[12] and the contribution of such signals to image quality is negative, according to their analysis. The image of a 25 cm rat obtained with ^{99m}Tc by a composite of individual images obtained each in 3 minutes is shown in Fig. 5.

The detectors for an array formed by two high-purity Ge elements placed together, forming a 32 x 16 cell matrix have been completed by the Livermore group and should be fully operational in the near future.

P. A. Schlosser, et al[24] at the Ohio State University have demonstrated the feasability of fabricating high-purity Ge orthogonal strip detectors with a charge-splitting resistor network for readout. Using a 10 x 10 cell arrangement, with 2 mm cell spacing (2 cm x 2 cm element) and 5 mm thickness, those workers have measured a best energy resolution of 5.5 KeV FWHM and a spatial resolution of 1.66 mm FWHM in their system. The projection as to the performance of an improved full size camera of 15 x 15 cm is an energy resolution of 3.3 KeV FWHM and a spatial resolution of 2.2 mm FWHM by using optimized filtering.

Strauss, et al[25] have examined the performance of a different type of camera based on a coaxial Ge(Li) detector with a circular active face. Positional information is obtained in polar coordinates by dividing the circle into narrow wedges (angular information) and using the different pulse shapes obtained for the detector current signal depending on the distance from the detector center of the point of gamma-ray interaction (radial information). The tests were limited to proving the fundamental properties of Ge as an image detector. High spatial resolution, excellent scatter rejection and the ability to separate isotopes were well demonstrated. Substantial distortion of the image shapes was obtained, however, and this is attributed to non-linearity in the electronics. The authors do not

emphasize the design of the camera as a prototype for a larger instrument at this time.

Both the charge splitting resistor network multielement camera and the circular coaxial camera suffer from position information degradation when Compton scattering occurs in the detector, just as it was the case in the delay line readout scheme. It appears that the only way to avoid this problem is to have independent amplifiers for each orthogonal strip and an anti-coincidence circuit configuration. This degradation effect becomes increasingly important when imaging higher energy isotopes.

II. FLUORESCENCE SCANNING

Imaging by fluorescence scanning was first reported by Hoffer, et al[26] as a technique allowing the imaging of the distribution of moderately high atomic number tracers existing naturally or taken up by shallow organs after injection. The authors demonstrated good delineation of the human thyroid by fluorescence of the natural iodine in it and showed the complementarity of the procedure with radioactive iodine scans. By using a suitable configuration, laminographic information can as well be obtained. A radioactive source and a Si(Li) detector were used for the iodine imaging. Barium was also used to image the liver of a mouse although the concentration attained would have been insufficient for satisfactory visualization by conventional radiography. For X-ray energies above 40 KeV, the authors recommended using Ge detectors because of their higher efficiency.

Brill, et al[20] have used Ge detectors of relatively small size for tumor localization by fluorescence imaging of stable tracers. In particular, they have explored the possibility of fluorescing bismuth taken up by a tumor in realistic concentrations and found the technique promising, although more efficient Ge detectors would be a necessity for success in a clinical situation.

Further work on the development of the technique is reported by Hoffer, et al,[27] Patton, et al[28], Kaufman, et al[29], the latter one showing a quantitative technique for the absolute determination of tracer element contents based on the ratio K_α to K_β.

The differentation between malignant and benign solitary thyroid nodules by fluorescent scanning has been investigated by Patton, et al[30]. Based on the clinically determined fact that the ratio of iodine content of malignant

nodules to the content of a normal equal thyroid area is below 0.6, those authors have developed a technique with malignancy predictive value of 79% on the basis of their preliminary work. Figure 6 describes the principles of the technique. A solitary cold nodule in a fluorescent scan (A) is marked visually. An equal size image is generated by computer (B) and superimposed on to the fluorescent scan image (C) in order to determine the coordinates of nodule region (2D) and those of the contralateral normal area (1D). The iodine contents ratio is then computed from the scan data. The ratios determined in that fashion for 42 patients grouped by the nature of their nodules is shown in Fig. 7. Groups are based on histologic study of surgical specimens. Finally, a plot of invivo vs. invitro iodine contents ratio from 14 patients with solitary 'cold' thyroid nodules is shown in Fig. 8, showing a correlation coefficient of 0.93.

III. CONCLUSIONS

The use of high-resolution semiconductor detectors in nuclear-medicine imaging is establishing itself without much controversy in applications in which a single detector with reasonably simple electronics can perform a clincically useful task, as is the case with Fluorescence Scanning. In the application to radioisotope imaging, it appears that one should divide any attempt at judging germanium detector systems into two parts: 1) research medicine and 2) routine clinical applications. In the case of research medicine a physician and/or patient may be willing to put up with a detector system of lower efficiency or higher cost than a conventional NaI system in exchange for the ability to image regions which would otherwise be very hard or impossible to image, or for multiple isotope work. The technology for producing such instruments exists and a growth in the use of Ge scanners and cameras can be expected in research centers. For routine clinical applications in which patient imaging time is a very important factor and where the cost, availability and maintenance of a complex germanium system may present some problems, at least for some time, it appears less likely that the improved imaging capabilities of germanium will represent a dramatic enough change over the best NaI systems to lead one to expect a general change to germanium detectors.

REFERENCES

1. Goulding, F. and Y. Stone, Semiconductor Radiation Detectors, in "Semiconductor Detectors in the Future of Nuclear Medicine, Hoffer, Beck and Gottschalk, Eds., The Society of Nuclear Medicine, Inc. New York (1971) Chapter 1.
2. Armantrout, G. A., Principles of Semiconductor Detector Operation, in "Semiconductor Detectors in the Future of Nuclear Medicine, Hoffer, Beck and Gottschalk, Eds., The Society of Nuclear Medicine, Inc. New York (1971) Chapter 2.
3. Bradley, A.E., Fundamentals of Semiconductor Detector Systems Design, in "Semiconductor Detectors in the Future of Nuclear Medicine, Hoffer, Beck and Gottschalk, Eds., The Society of Nuclear Medicine, Inc., New York (1971) Chapter 3.
4. Baertsch, R.D. and R. N. Hall, Gamma Ray Detectors from High-Purity Germanium, IEEE Trans. Nucl. Sci. NS-17, No. 3 (1970) p. 235.
5. Llacer, J., Planar and Coaxial High-Purity Germanium Detectors, Nucl. Instr. and Methods 98 (1972) p. 259.
6. Llacer, J., A Large Volume High-Purity Germanium Radiation Detector, Nucl. Instr. and Methods 104 (1972) p. 249.
7. Pehl, R. H., R. C. Cordi, and F. S. Goulding, High-Purity Germanium: Detector Fabrication and Performance, IEEE Trans. Nucl. Sci. NS-19 No. 1 (1972) p. 265.
8. Hansen, W.L. and E. E. Haller, A View of the Present Status and Future Prospects of High-Purity Germanium, IEEE Trans. Nucl. Sci. NS-21, No. 1 (1974) p. 251.
9. Marler, J. M. and P. Hewka, Coaxial Detectors from High-Purity Germanium, IEEE Trans. Nucl. Sci. NS-21, No. 1 (1974) p. 287.
10. Hall, R. N. and T. J. Soltys, Radial Gradient Coaxial Detectors, IEEE Trans. Nucl. Sci. NS-23, No. 1 (1976) p. 88.
11. Beck, R. N., L. T. Zimmer, D. B. Charleston, P. B. Hoffer and N. Lembares, The Theoretical Advantages of Eliminating Scatter in Imaging Systems, in "Semiconductor Detectors in the Future of Nuclear Medicine, Hoffer, Beck and Gottschalk, Eds., The Society of Nuclear Medicine, Inc., New York (1971) Chapter 7.

12. Strauss, M.G. and I. S. Sherman, Imaging Efficiency of Ge and NaI(Tl) Gamma-Ray Detectors, IEEE Trans. Nucl. Sci., NS-22, No. 1 (1975) p. 331.
13. Kraner, H. W., J. Llacer and H. L. Atkins, A Large-Area Germanium Detector for Rectilinear Scanning, Radiology, 106, No. 2 (1973) p. 425.
14. Llacer, J., Ultimate Capabilities of Detectors with High-Energy Resolution in Radioisotope Scanning, IEEE Trans. Nucl. Sci. NS-20, No. 1 (1973) p. 273.
15. Llacer, J. and L. S. Graham, The Effect of Improving Energy Resolution on Gamma Camera Performance: A Quantitative Analysis, IEEE Trans. Nucl. Sci. NS-22, No. 1 (1975) p. 309.
16. Hoffer, P. B. and R. N. Beck, Effect of Minimizing Scatter Using Ge(Li) Detectors on Phantom Models and Patients, in "Semiconductor Detectors in the Future of Nuclear Medicine", Hoffer, Beck and Gottschalk, Eds., The Society of Nuclear Medicine, Inc., New York (1971) Chapter 9.
17. Kirby, J. A., P. L. Phelps, D.L. Sawyer, G.A. Armantrout, and R. N. Beck, A High Efficiency Multidetector System for Tumor Scanning, IEEE Trans. Nucl. Sci., NS-23, No. 1 (1976) p. 543.
18. Beck, R. N., L. T. Zimmer, D. B. Charleston, W. W. Shipley and B. S. Brunsden, A Theory of Optimum Utilization of All Detected Radiation, in "Semiconductor Detectors in Medicine", U.S. A.E.C., Office of Information Services, Technical Information Center, CONF-730321 (1973) p. 87.
19. Glass, H. I., F. R. Hudson, M. T. French and J. P. Lavender, A 70 mm Diameter Germanium Detector Medical Radioisotope Scanner, IAEA Proc. Symp. on Medical Radioisotope Scintigraphy, Monte Carlo, 1972. IAEA, Vienna, 1973, Vol. 1, p. 79.
20. Brill, A. B., J. Patton, R. Price and C. V. Flanigan Cosik, Applications of High Resolution Semiconductor Detectors in the Evaluation of Tumor Localizing Agents, IAEA Proc. on a Medical Radioisotope Scintigraphy, Monte Carlo, 1972. IAEA, Vienna, 1973, Vol. 1, p. 217.
21. Parker, R. P., E. M. Gunnersen, R. Ellis and J. Bell, A Semiconductor Gamma-Camera, Assesment of Results, IAEA Proc. Symp. on Medical Radioisotope Scintigraphy, Monte Carlo, 1972. IAEA, Vienna, 1973, Vol. 1, p. 193.

22. Detko, J. F., Progress Toward a Stable Orthogonal Strip Germanium Gamma Camera, IEEE Trans. Nucl. Sci. NS-23, No. 1 (1976), p. 538.

23. Kaufman, L., R. Hattner, D. Price, S. Swann, J. Huberty, G. Armantrout, D. Camp, J. McQuaid and J. Ewins, Imaging with a Small Ultra Pure Germanium Gamma Camera, IEEE Trans. Nucl. Sci. NS-22, No. 1 (1975) p. 395.

24. Schlosser, P. A., D. W. Miller, M. S. Gerber, R. F. Redmond, J. S. Harpster, W. J. Collis and W. W. Hunter, Jr., A Practical Gamma-ray Camera System Using High-Purity Germanium, IEEE Trans. Nucl. Sci. NS-21 No. 1 (1974) p. 658.

25. Strauss, M. G., I. S. Sherman, R. Brenner, and F. R. Lenkszus, Performance of a Coaxial Gamma-ray Camera, Journ. Nucl. Med., 15, No. 12, (1974) p. 1196.

26. Hoffer, P. B., Charleston, D. B., R. N. Beck and A. Gottschalk, Fluorescent Scanning, A New Investigative Technique, IAEA Proc. Symp. on Medical Radioisotope Scintigraphy, Monte Carlo, 1972. IAEA, Vienna, 1973, Vol. 1 p. 261.

27. Hoffer, P. B. C. Bekerman, J. Bowie and R. Beck, Fluorescent Thyroid Scanning, What is New, in "Semiconductor Detectors in Medicine", U.S. A.E.C., Office of Information Services, Technical Information Center, CONF-730321 (1973) p. 238.

28. Patton, J. A., A. B. Brill, G. Blanco and R. Highfill, Experience with Semiconductors in Imaging and Functions Studies at Vanderbilt, in "Semiconductor Detectors in Medicine", U.S.A.E.C., Office of Information Services, Technical Information Center, CONF-730321 (1973) p. 254.

29. Kaufman, L., C. J. Wilson, J. A. Nelson and D. M. Shames, Techniques for In Vitro and In Vivo Elemental Quantification by Fluorescent Excitation, in "Semiconductor Detectors in Medicine", U.S.A.E.C., Office of Information Services, Technical Information Center, CONF-730321 (1973) p. 127.

30. Patton, J. A., J. W. Hollifield, A. B. Brill, G. S. Lee and D. D. Patton, Differentiation Between Malignant and Benign Solitary Thyroid Nodules by Fluorescent Scanning, J. Nucl. Med., Vol. 17, No. 1 (1975) p. 17.

FIGURE CAPTIONS

Fig. 1. Direct comparison of NaI(b) and Ge(Li)(g) phantom scans using 7 cm overlying lucite absorber at equal scanning speeds, equal scanning times. Scan parameters: line separation 2.25 mm, scan speed 29 cm/min, maximum counts per cm of scan: NaI = 1.72×10^3, Ge = $.83 \times 10^3$, recording lamp relative density: NaI = 1, Ge = 2. Collimator 1045 hole, 3.4 cm thick.

Fig. 2. MTFs as a function of energy acceptance window, W, and computer generated images of 70% activity cool spots of 1 cm and 0.5 cm diameter in a 9 cm circle of 100% activity as a function of W. Collimation to source distance Z = 7.3 cm, absorber thickness = 5 cm tissue equivalent, ^{99m}Tc.

Fig. 3. ^{99m}Tc brain scans in patient with known carcinoma in breast and suspected cerebral metastasis. A is brain scan with NaI detector, with a lesion observed in right occipital region. B is scan with Ge detector, with 'donut' lesion in right occipital region. Second lesion is seen in right motor area.

Fig. 4. ^{99m}Tc brain scans made in patient with suspected tumor, choroid plexus blocked with perchlorate. A scan with NaI detector shows apparent lesion in left posterior temporal region. B scan with Ge detector shows a linear density in the same region which communicates with the left lateral sinus and was interpreted as normal vascular structure.

Fig. 5. Image of a 25 cm rat injected with 9 mCi of ^{99m}Tc pyrophosphate, imaged on hour post-injection with a parallel hole tantalum/tungsten collimator. Each 2 x 2 cm unit in this composite was accumulated in a 3 minute period. This would be the time needed to obtain this image (10^6 counts) with a full size camera. Note the almost complete lack of scattered radiation from soft tissues.

Fig. 6. Schematic description of technique for determination of iodine contents ratio. (A) marking of nodule in photoplot. (B) computer generations of same-size image. (C) overlay of both images to determine coordinates of nodule, (2D), and of the corresponding normal contralateral area (1D). ICR = iodine contents in region 2/ i.c. in region 1.

Fig. 7. Iodine contents ratios determined before surgery on 42 patients with solitary 'cold' thyroid nodule. Groupings are based on hystologic study of surgical specimens.

Fig. 8. Plot of in vivo ICR determined by fluorescent scanning against in vitro ICR determined chemically in surgical specimens from 14 patients with solitary 'cold' thyroid nodules.

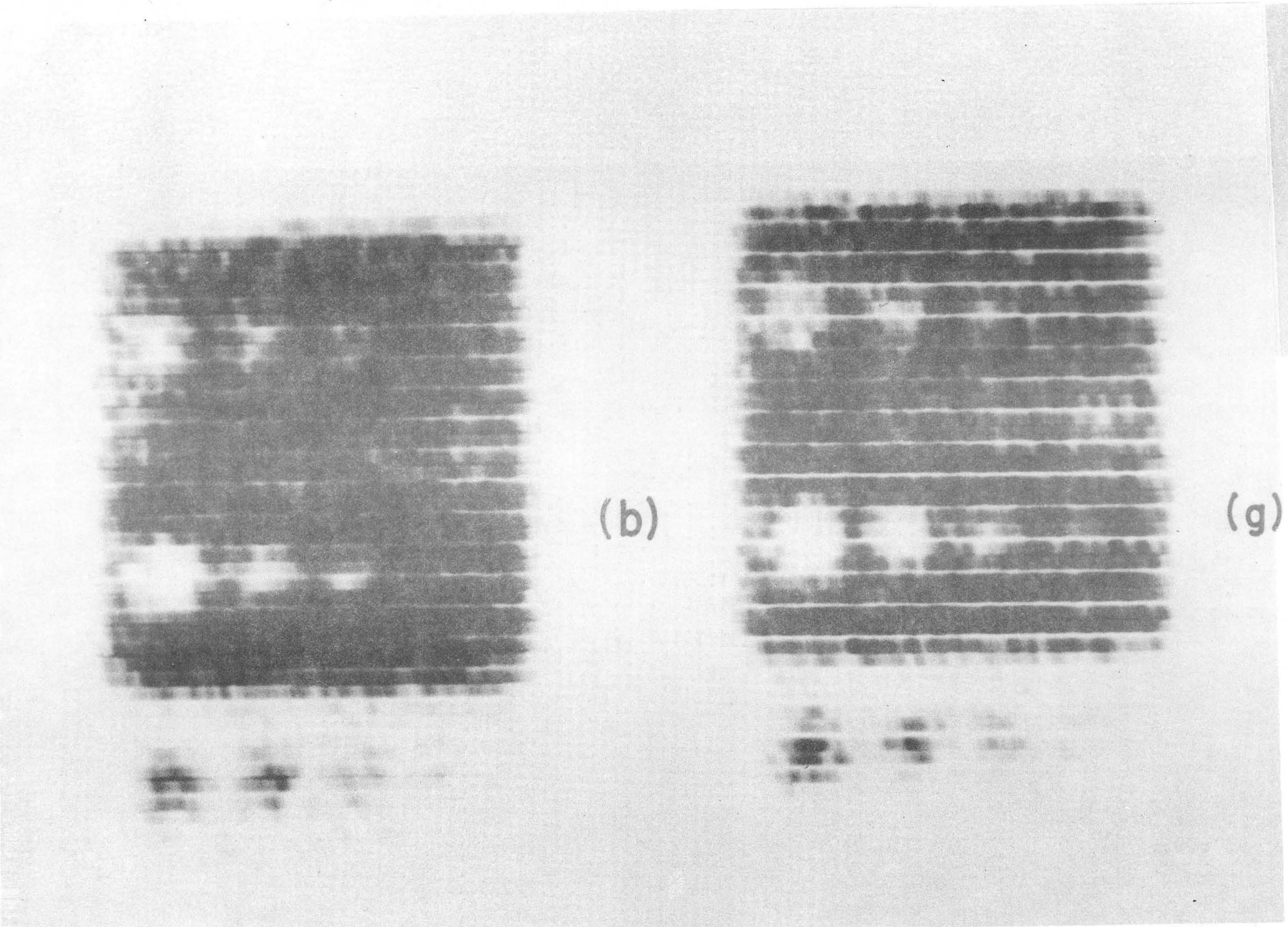

XBB 765-4395

Fig. 1

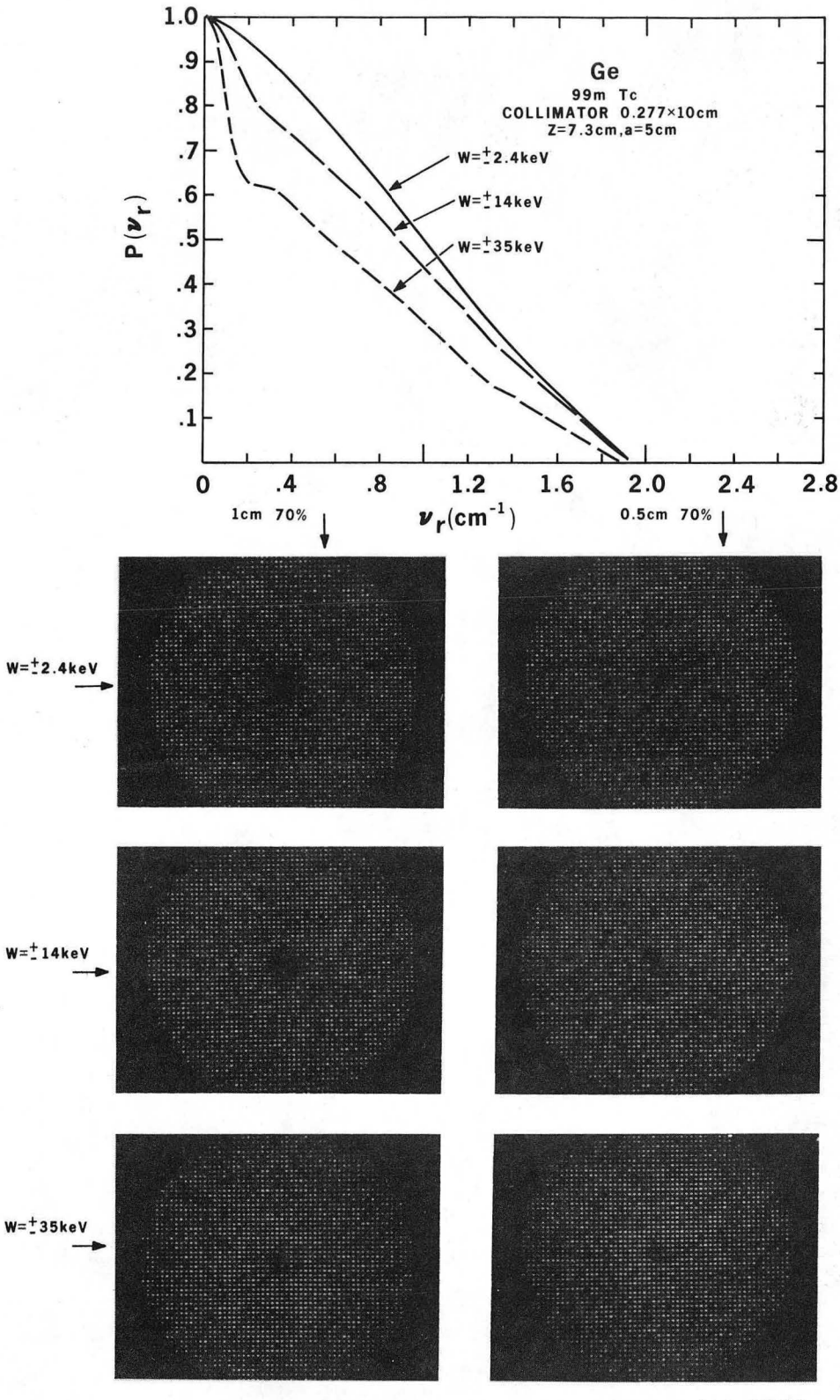

XBB 7410-7020

Fig. 2

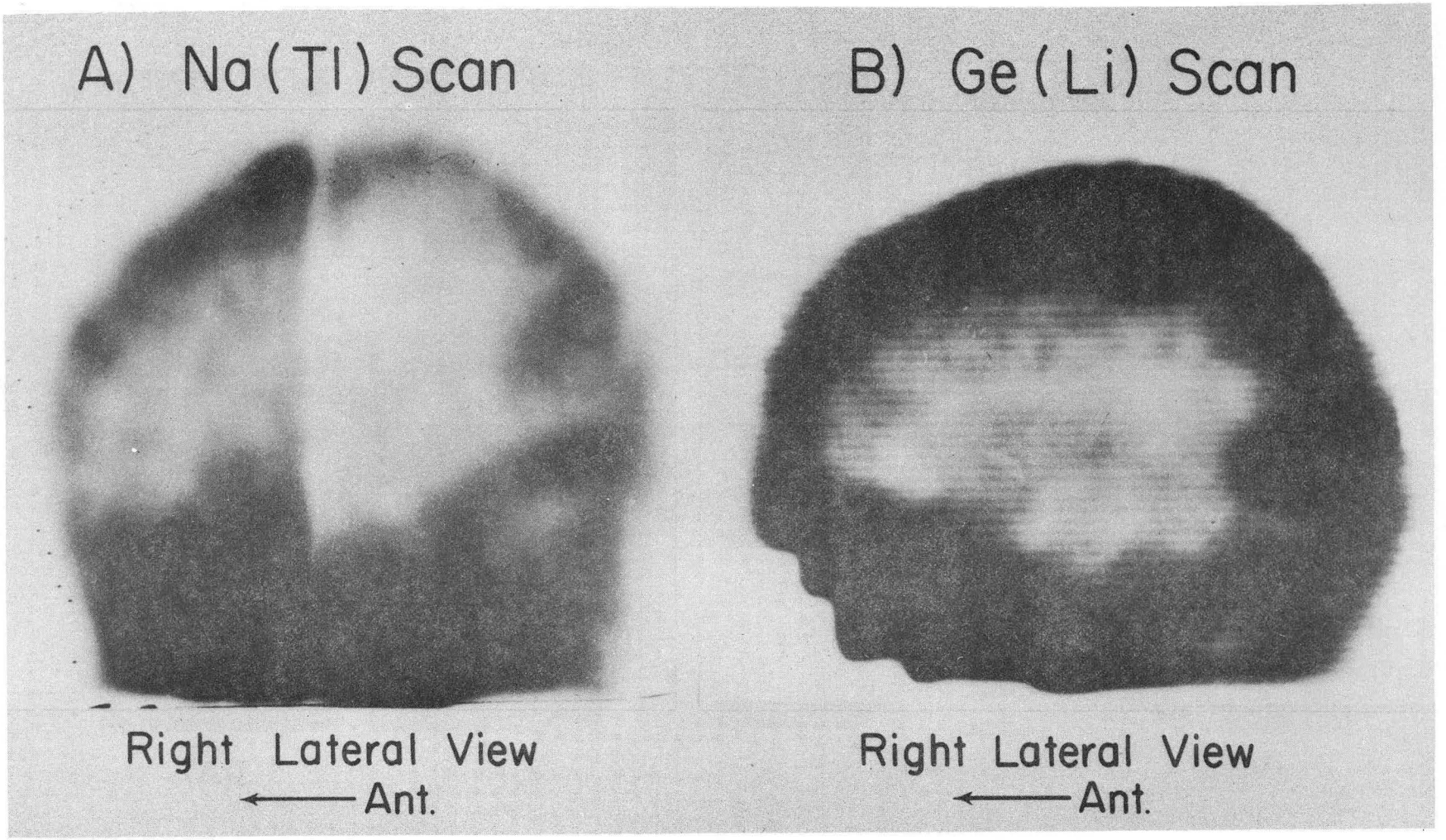

XBB 765-4397

Fig. 3

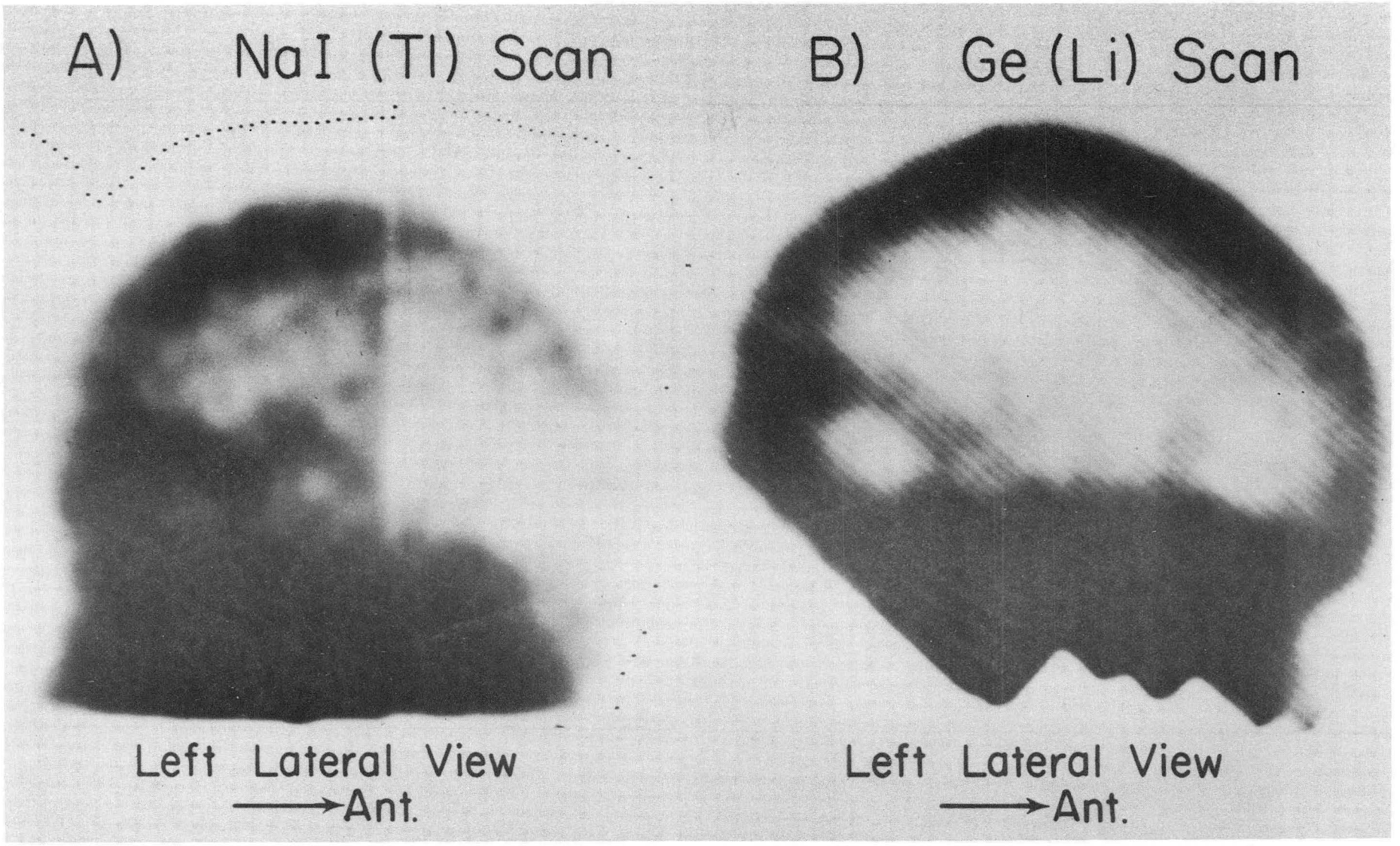

Fig. 4

XBB 765-4399

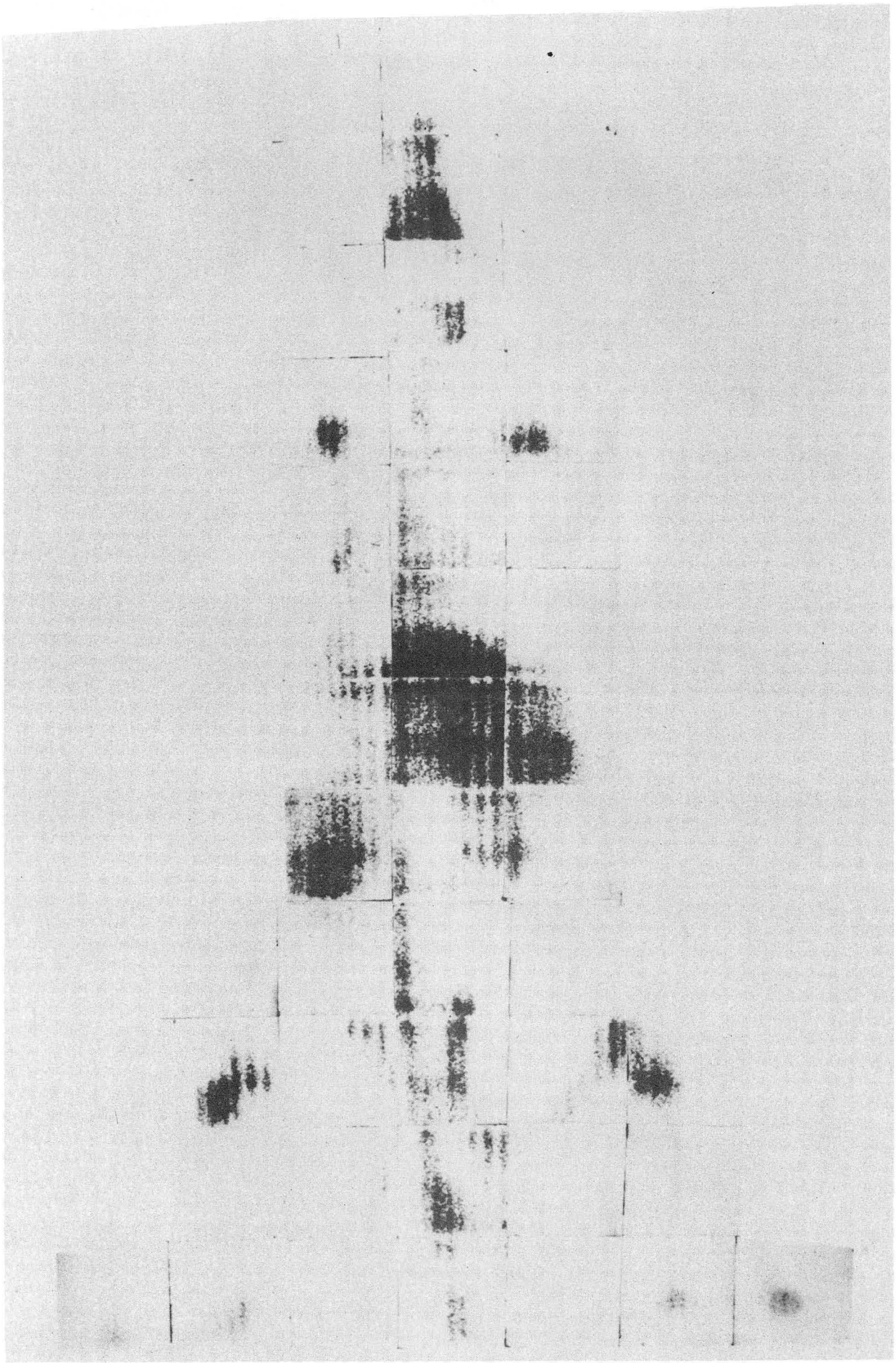

Fig. 5 XBB 765-4396

Fig. 6

XBB 765-4398

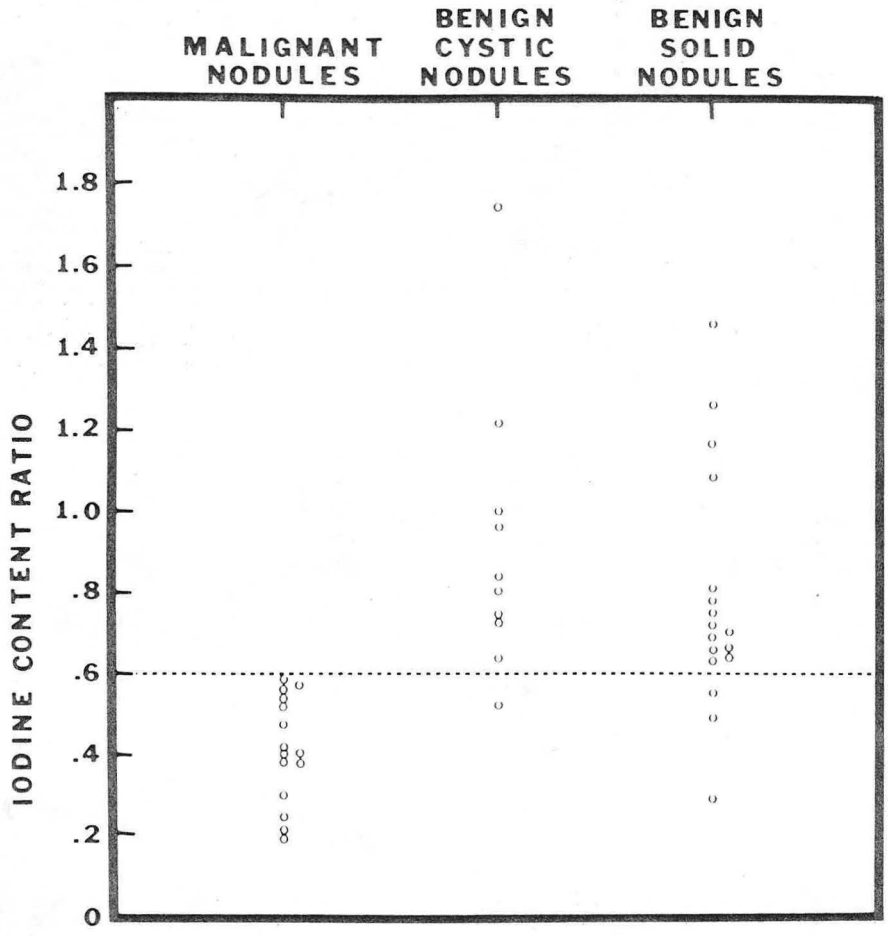
MALIGNANT NODULES
BENIGN CYSTIC NODULES
BENIGN SOLID NODULES
IODINE CONTENT RATIO
1.8
1.6
1.4
1.2
1.0
.8
.6
.4
.2
0

Fig. 7

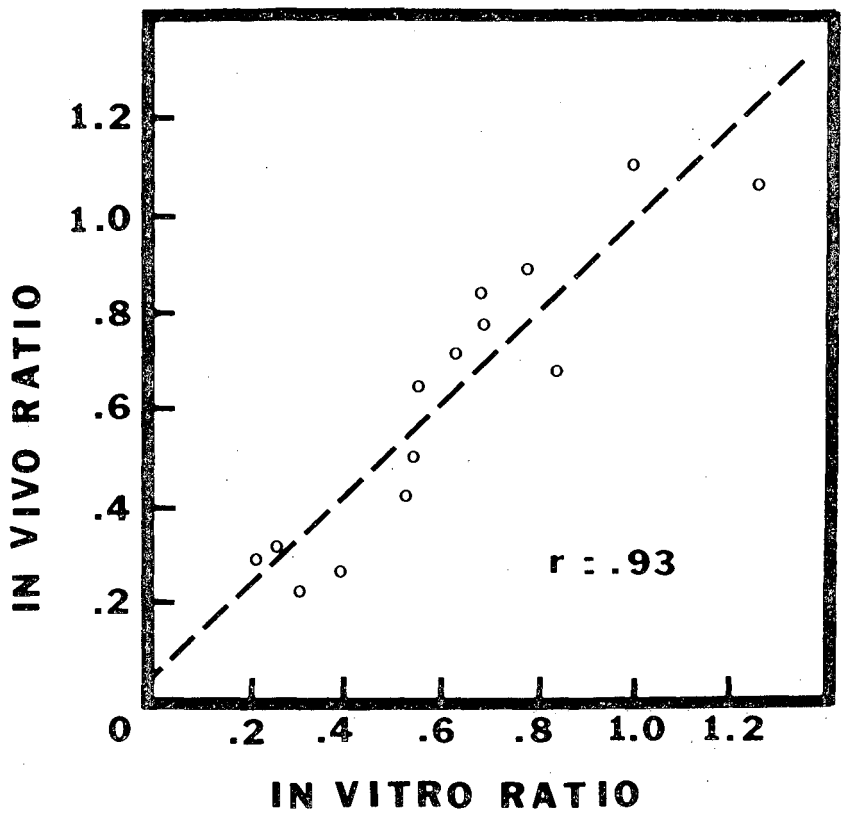

Fig. 8

TECHNICAL INFORMATION DIVISION
LAWRENCE BERKELEY LABORATORY
UNIVERSITY OF CALIFORNIA
BERKELEY, CALIFORNIA 94720

Submitted to Nuclear Instruments & Methods

LBL-4890
c. 2

TEST OF A LEAD-LIQUID ARGON ELECTROMAGNETIC SHOWER DETECTOR.

Hitlin, D.

May 1976

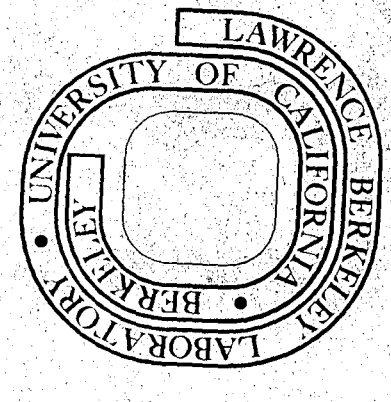

DISCLAIMER

SLAC-PUB-1761
LBL-4890
May 1976
(E/I)

TEST OF A LEAD-LIQUID ARGON ELECTROMAGNETIC SHOWER DETECTOR*

D. Hitlin, J. F. Martin and C. C. Morehouse

Stanford Linear Accelerator Center
Stanford University, Stanford, California 94305

and

G. S. Abrams, D. Briggs, W. Carithers, S. Cooper,
R. DeVoe, C. Friedberg, D. Marsh, S. Shannon,
E. Vella and J. S. Whitaker.

Lawrence Berkeley Laboratory and Department of Physics
University of California, Berkeley, California 94720

ABSTRACT

The design and construction of two lead-liquid argon electromagnetic shower detectors are described. Test results in beams of electrons and π^- of momenta .125 - 4 GeV/c and 1 - 4 GeV/c respectively are presented. Measurements were made of the energy resolution for electromagnetic showers, the position resolution, the behavior of the device in a transverse magnetic field and the radial and longitudinal characteristics of energy deposition, especially as they apply to π^-/e^- discrimination.

(Submitted to Nuclear Instruments & Methods)

*Work supported by the Energy Research and Development Administration.

28

1. Introduction

The recent development of liquid argon ionization chambers for hadron calorimeters and electromagnetic shower counters has made it possible to equip large 4π detectors at storage rings with electromagnetic detectors which have both good spatial and energy resolution. We will describe tests of small ionization chambers with thin lead radiators divided into 2 cm. wide strips. The results of these tests have been sufficiently encouraging for us to design a large system of ten modules which will provide the electromagnetic detection capability of the new SPEAR Mark II Detector Facility at SLAC.

The use of liquid argon to sample the ionization produced in a hadronic or electromagnetic cascade was pioneered by Willis. An excellent introduction to these devices is provided in the papers of Willis and Radeka[1], Engler, et al.,[2] and Knies and Neuffer[3]. We will therefore not dwell on details of the theory of the device or the associated electronic circuitry.

2. Design and Construction

A lead/liquid argon device measures the energy of a shower by sampling the total ionization energy loss of the shower products. On the basis of electromagnetic shower theory one would expect the device to be linear[4] if all the shower energy is contained, and the distribution of sampled tracks to be nearly Gaussian with an r.m.s. width (energy resolution) inversely proportional to the square root of the plate thickness ($\sigma \sim t^{-\frac{1}{2}}$). Since there are a large number of very low energy particles in the shower, this approximation will not be valid below a given plate thickness. Monte Carlo studies indeed indicate

that for a sampling device with alternate layers of lead and liquid argon, the resolution at 1 GeV/c does improve as $t^{-\frac{1}{2}}$ in the region down to plate thicknesses of ~.2 r.l., but then improves more quickly for finer sampling (see Figure 1).

In order to test the dependence of resolution on sampling thickness, as well as to try different construction techniques and readout schemes, two modules were constructed. Both used 2 cm. wide readout strips, with all strips oriented in the same direction. The active volume of both modules was 23 cm. x 24.5 cm. x ~30 cm. deep.

In the first detector (henceforth A) a unit cell consisted of a 1.1 mm. Pb sheet, 2 mm. of liquid argon, a 2.3 mm. Pb/G10 laminate with the lead segmented into 2 cm. strips, and 2 mm. of liquid argon. Detector A was constructed of 42 such unit cells for a total depth of 15.75 r.l. Each laminate consisted of 11 lead strips, 2 cm. wide x 0.42 mm. thick, glued (with 3M #3549 Structural Adhesive) to both sides of a 1.2 mm. thick sheet of NEMA G10 fiberglass. (This lamination technique was found to have sufficient shear strength to withstand the differential contraction of at least 3 meters of Pb/G10 sandwich at liquid nitrogen temperature). Ceramic washers maintained the 2 mm. gap spacing. The entire structure was clamped together from the outside corners. The Pb sheets were at ground, and the lead strips were at negative high voltage, the signal being coupled out through 0.01 μf capacitors.

For the second module (henceforth B) the solid planes were 2.2 mm. Pb sheets and the 2 cm. wide readout strips were constructed from etched copper-clad G10 circuit board material. The structure was clamped with

threaded G10 rods and the 2 mm. gap spacing was maintained with ceramic washers. This device consisted of 36 unit cells and was also 15.75 r.l. deep. In this module the solid sheets were connected to high voltage and the signal was taken from the printed circuit strips at ground. Decoupling was accomplished at each solid plate through a 0.01 μf capacitor. The electrical performance of the two modules was essentially identical, but the second scheme of high voltage distribution requires fewer large capacitors.

Sixteen channels of readout electronics were constructed; unit cells in both modules were therefore grouped together as shown in Figure 2. This configuration was chosen to allow the study of longitudinal and radial energy deposition in some detail, especially as they pertained to the spatial resolution and π/e rejection capability of the device. The capacitance of the individual channels varied from 200pf to 2400pf. Signals were carried to a feedthrough with short lengths of RG174 coaxial cable.

The preamplifiers, mounted directly on the dewar, were of a design used by the Willis group at CERN[5], with some minor changes. For ease of winding, Ferroxcube 3D3 pot cores were used for the input transformer in place of the toroidal type used by Willis. The low noise FET used was a selected TIS75. Sixty percent of a sample of 100 of these inexpensive FET's were found to have a noise figure of $\leq$ 1.1 nV/$\sqrt{\text{Hz}}$ at 100 kHz. The preamplifiers drove twisted pair lines to bipolar shaping amplifiers, also of a design used by Willis. With a shaping time of 0.6 μsec, the equivalent noise charge varied from 4,000 r.m.s. electrons for channels with 200pf capacitance to 12,000 r.m.s. electrons for 2400pf

channels. The outputs of the shaping amplifiers were digitized in LeCroy #2249 ADC's, gated for ± 75 nsec about the peak.

Relative calibration of the gain of each of the sixteen channels was accomplished by applying a long pulse of known amplitude to small (10pf per 200pf of channel capacitance) silver mica capacitors mounted within the dewar close to each strip group. The input pulse was varied over a range of 15 mV ($\sim 10^6$ electrons for a 10pf calibration capacitor) and the ADC output was recorded for each step. The long term stability of the electronics was found to be better than 1%.

The modules were contained in an upright stainless steel dewar 150 cm. deep by 45 cm. inside diameter. The dewar had an entrance port for the beam consisting of 0.5 mm. of stainless steel in two windows and 2 cm. of liquid argon, for a total of 0.1 r.l. The fill cycle began with several cycles of alternately filling with argon gas and evacuating to 50 microns. Argon gas was condensed with a heat exchanger coil filled with liquid nitrogen. The argon used was either "Pre-purified" grade gas or the boiloff from 130 liter dewars of welding grade liquid argon. Approximately 75 liters of liquid were needed to cover the module assembly. Regulation of the argon space pressure (approximately 1 psig) was accomplished by controlling the liquid nitrogen flow through the heat exchanger, which consisted of 5 meters of copper tubing. During the fill and at regular intervals througout the test, the oxygen impurity in the argon gas in equilibrium with the liquid was tested by measuring the burnout time of small tungsten filaments[6]. The oxygen contamination at fill time was less than 0.1 ppm, and remained at this

level for periods of weeks. No purification of the argon was found to be necessary and none was attempted.

3. Test Results

The modules were tested at SLAC in an e^- beam from .125 to 4 GeV/c and a π^- beam from 1 to 4 GeV/c. For tests at 1 GeV/c and above, π's and e's were selected by changes in the target and production angle, by the introduction of lead at the first focus of the beam, and with the use of two Freon 13 filled threshold Cerenkov counters placed upstream of the dewar. Each of the Cerenkov counters was measured to be more than 99% efficient on electrons. The momentum spread of the beam, 1.8% (FWHM) above 1 GeV/c, increasing to 3% at .125 GeV/c, was negligible.

The modules were large enough to contain electromagnetic showers in the radial direction at all relevant energies and to have 97% containment in the longitudinal direction at 4 GeV/c.. This resulted in a response which was linear at low energies, with a slight deviation only at the highest energy point, as shown in Figure 3. The curve is a linear fit to the data up to 2 GeV/c. The energy loss of non-interacting π^- is also shown. No significant change in energy loss for pions is observed between 1 and 4 GeV/c.

While we were most concerned with the energy resolution of the detectors for photon initiated showers, it is most practical to test them in an electron beam. The energy resolution for low energy electrons is substantially degraded by energy loss in material in front of of the detector. We studied this effect by placing aluminum blocks in the beam just upstream of the detector. For the tests of module B, in

addition to the 0.1 r.l. of the dewar entrance window, the electrons traversed about 0.1 r.l. in beam defining scintillation counters and 0.25 r.l. in the two Cerenkov counters. For the tests of module A below 1 GeV/c, the Cerenkov counters were removed. In order to obtain the inherent energy resolution of the devices, the measurements with additional Al in the beam were used to extrapolate to zero material before the detector. In addition, an electromagnetic shower Monte Carlo calculation was used to verify the extrapolation.

Figure 4 shows the measured resolution of module B for electrons of several momenta, with and without additional aluminum placed in the beam. The degradation in resolution due to energy loss before the detector is clearly more pronounced at lower energies. The measurements were used to extrapolate to the expected resolution for photons. For module A below 1 GeV/c, the corresponding corrections were smaller.

Figure 5a shows the measured resolution for module A as a function of electron momentum. The dashed curve is the result of a Monte Carlo shower calculation of the energy deposited in the argon of a detector with alternate layers of lead and liquid argon preceded by .25 r.l. of Al. The solid curve is the sum in quadrature of the shower calculation and the total of 12 MeV of measured r.m.s. electronic noise. Figure 5b shows the resolution of module A extrapolated to zero material upstream of the counter. The curve is again the sum in quadrature of the Monte Carlo calculation, this time with no extra material in the beam, and the measured electronic noise. The fluctuations in the shower calculation are well represented by $6.5\%/\sqrt{E_e(\text{GeV})}$. Figure 5c shows the

resolution of module B extrapolated to zero additional material in the beam. The curve is the sum in quadrature of the Monte Carlo calculation, which is well represented by $9.5\%/\sqrt{E_e(\text{GeV})}$ and 12 MeV of electronic noise. The resolution of the two modules is consistent with $t^{-\frac{1}{2}}$ as expected from the calculations shown in Figure 1.

The energy response curves of module A at several electron monenta are shown in Figure 6 together with curves representing the best least squares fit of a gaussian. These represent the data well, with the exception of small low energy tails due to energy loss upstream.

It is possible to improve the low energy resolution of the device somewhat by using only the front part of the module, so as not to add unnecessary electronic noise. This is illustrated in Figure 7, where the resolution is shown as a function of the depth of the device utilized. It is seen that the test module is well matched to 1 GeV, but could have better resolution at high energy if fluctuations due to energy loss out the back were reduced. More importantly, the resolution at low energy can be improved by ignoring the last 4.5 r.l. of the module. This has not been done in the resolution vs. energy curves of Figure 5.

The longitudinal distribution of shower energy could be sampled in groups ending at 2.25,4.5,6.75,10.25 and 15.75 r.l. These distributions are shown for incident momenta of .25, 1 and 4 GeV/c in Figure 8. The expected logarithmic increase of shower maximum with energy is clearly evident. These curves make it clear that a shower detector intended for use below several GeV must incorporate electronics with a

wide dynamic range. This problem is further accentuated by the large fluctuations about the mean energy deposited at a given depth. Figure 9 shows the actual distribution of energy in each of the five depths at incident electron momenta of .25 GeV/c and 4 GeV/c. The curves at the two energies are normalized to 100% of the charge deposited at each energy separately, so that the 4 GeV/c scale is sixteen times that of the .25 GeV/c scale. It will be seen that the fluctuations of the .25 GeV/c curves are very large, such that it is not improbable that only a small amount of energy will be deposited after 4.5 r.l. Aside from the requirements this places on the dynamic range of a channel at a given depth, it is clear that a detector which is to be used to measure the position of the shower in this energy range must determine both coordinates and resolve ambiguities very early in the shower, typically in the first three or four radiation lengths. This is easily accomplished by interleaving different coordinate strips at the front of the module.

The data in Figures 3-9 were obtained with the high voltage set to 3 kV, or a field of 15 kV/cm. The operating plateau is very wide; signals can be seen at 250 volts. The collected charge and resolution for a 1 GeV/c e^- as a function of electric field for module A are shown in Figure 10.

Since some of the shower counter modules for the Mark II Detector will be placed in a transverse magnetic field of a few hundred gauss and in longitudinal fields of up to 5 kG, a test of the effect of a magnetic field on the charge collected and on the resolution of the module was made.

Calculations indicate that the device is not likely to be affected by reasonable fields, but the region of onset of measurable effects is sensitive to assumptions about the distribution of low energy shower tracks. Data were therefore taken for .25 GeV/c and 1 GeV/c electrons in a transverse magnetic field of up to 1.3 kG. The results at 1 GeV/c are shown in Figure 11. No significant effect was seen at either energy at any field.

The 2 cm. wide collection strips were grouped such that we obtained three samples of the transverse shower spread for each of the five depths. All of the strips were parallel; the shower distribution is projected onto a single transverse coordinate (x-axis). Since the electron beam size was larger than the expected spatial resolution, we measured the resolution on an event-by-event basis. Two methods were employed.

In the simpler method, the centroid and variance for the shower were computed in each of the five layers. A least squares fit of a straight line was then made to these five centroids, and the residuals in each layer were then found. The r.m.s. deviations are plotted for 1 GeV/c electrons in Figure 12. It is seen that a spatial resolution of a few millimeters is achieved with the present 2 cm. strip width. Figure 13 shows the actual distribution of the residuals in the first two radiation lengths for a 1 GeV/c electron.

The second method involved a fit to the pulse height distribution at each depth. For convenience, we assume a Gaussian shape and fit for the mean and width (x_i, σ_i) at each depth. A preliminary fit is made

for each depth and the resulting five means (x_i) are then fit to a straight line representing the electron direction. The Gaussian widths are then re-fit with the means constrained to the values given by the straight line fit. The results for this constrained fit are shown in Figure 14. The transverse width of the shower is independent of the electron energy over the region studied, although the fluctuations are of course larger at low energies.

The spatial resolution is given by the error in the mean for the Gaussian fit. To calculate this error, we must estimate the number of independent tracks at each depth in the shower. To obtain the estimate, we divide the total pulse height for each cell by the pulse height corresponding to a single minimum ionizing particle. The fit is then made with a maximum likelihood technique using Poisson statistics on the estimated number of independent tracks. The spatial resolution results for the uncorrelated error in the mean (Δx_i) are shown in Figure 15. We have made an independent check on our estimate of the errors by studying the χ^2 distribution for the straight line for the means. The χ^2 distributions show more events at smaller χ^2 than one would expect for three degrees of freedom indicating that our errors are slightly over-estimated or that correlations exist from depth to depth.

One of the most important functions of an electromagnetic shower detector is the separation of hadrons from electrons, and in particular, the identification of electrons in a large background of pions. The ratio of absorption length to radiation length is large for a lead-liquid argon detector, (typically 25-30) and the counter is easily subdivided longitudinally and radially to measure the different characteristics of

hadronic and electromagnetic showers. Results on proton/electron separation have been recently reported by Engler, et al.[7], for a detector similar to those discussed here.

Our tests involved π^- and e^- at 1,2 and 4 GeV/c, with and without 1 r.l. of Al in front of the device to simulate the effects of a solenoid coil. Although it is possible to use maximum likelihood techniques to effect the π^-/e^- separation, we have confined ourselves here to a series of simple orthogonal cuts on total energy deposition, and on the longitudinal and radial deposition of shower energy. At energies above 1 GeV/c the primary means of e^-/π^- discrimination is comparison of the total energy deposition in the device. This is shown for 2 GeV/c e^- and π^- in Figure 16. Study of the energy division between the front and back of the detector can improve the separation markedly, however, especially at low energies. The distribution of charge in the first two radiation lengths ($Q_{1,2}$) *vs.* the total (Q_{tot}) was studied, as was the distribution of charge in the first four radiation lengths (Q_{1-4}) *vs.* the total. There is also a difference between the radial spread of hadronic and electromagnetic showers, which can be used to gain a slight improvement in π/e separation, although a drastic improvement in separation can only be achieved at the expense of electron efficiency. Figure 17 shows a scatterplot of the energy deposited in the first two radiation lengths *versus* the r.m.s. deviation of the distribution of charge among three of the 2 cm. strips ($\sigma^2 = \Sigma\, Q_i\, (x - \bar{x})^2 / \Sigma\, Q_i$), for 4 GeV/c π^- and e^-. It will be seen that those π^- with large $Q_{1,2}$, i.e., those which interact in or before the first two radiation lengths tend to have a larger σ. Thus a cut on the maximum variance

can remove some π^-, but a cut which removes a large number of π^- necessarily sharply reduces electron efficiency. Our devices measured only a single projection of the shower; cuts on both transverse projections would improve the π/e rejection somewhat. In Figures 18,19 we show scatterplots of $Q_{1,2}$ vs. Q_{tot} and Q_{1-4} vs. Q_{tot}. This data has already been cut on maximum $\sigma_{1,2}$ or σ_{1-4}. Clearly, most of the π/e rejection comes from the differences in Q_{tot} but substantial improvement in rejection can be achieved by also using the differences in energy deposition in the front of the detector. Figure 20 summarizes the power of these cuts for data with and without 1 r.l. of aluminum before the detector. Since π^- charge exchange amounts to ~1% in 1 r.l. of Al at these energies, the π^-/e^- rejection ratio does suffer somewhat with the additional material. Without the Al, it is possible to achieve a π^- efficiency as low as 7×10^{-3} with 90% electron efficiency at 1 GeV/c. At higher energies substantially better separation can be achieved.

4. Conclusion

Measurements of the energy resolution, spatial resolution, hadron/electron separation capability and other characteristics of a lead-liquid argon electromagnetic shower counter have been presented. The performance of the device has encouraged us to adopt this technique for shower detection in the Mark II Detector Facility at SPEAR.

We wish to thank W. J. Willis, J. Lindsey, V. Radeka and other members of the IMP Group for helpful conversations, R. Gearhart for his efforts in establishing the low energy beams required for these tests, and D. Hunt and R. Fuzesy for the design and construction of the cryogenic system.

REFERENCES

1. W. J. Willis and V. Radeka, Nucl. Instr. and Meth. 120, 221 (1974).
2. J. Engler, B. Friend, W. Hofmann, H. Keim, R. Nickson, W. Schmidt-Parzefall, A. Segar, M. Tyrrell, D. Wegener, T. Willard and K. Winter, Nucl. Instr. and Meth. 120, 157 (1974).
3. G. Knies and D. Neuffer, Nucl. Instr. and Meth. 120, 1 (1974).
4. B. Rossi, High Energy Particles (New York, Prentice Hall, 1952).
5. Thanks are due to W. J. Willis, J. Lindsey and V. Radeka for their aid in duplicating their preamp and shaping amplifier circuitry.
6. Designed by E. Hoyt and W. P. Schulz, SLAC Physical Electronics Grp.
7. J. Engler, W. Hofmann, J. Spengler and D. Wegener, Karlsruhe preprint, 1976.

FIGURE CAPTIONS

1. Dependence of resolution on plate thickness for 1 GeV/c electrons in a sampling detector with lead plates. Curve a shows the $t^{-\frac{1}{2}}$ dependence expected from analytic shower theory. Curve b is the result of a Monte Carlo shower calculation. σ is the r.m.s. deviation of the ionization energy deposited in 2 mm. gaps of liquid argon. The total depth of the device was held constant at 16 radiation lengths.
2. Grouping of channels in width and depth in the test modules. All groups consisted of 2 cm. wide strips running in the vertical direction only.
3. Collected charge in minions (1 minion = charge collected for the passage of a minimum ionizing particle through a minimum grouping of cells, i.e., through six gaps) vs. momentum of incident e^- and (non-interacting) π^-.
4. Energy resolution of module B for electron momenta from .25 to 4 GeV/c as a function of the amount of aluminum placed upstream of the detector.
5. a) Measured resolution of module A as a function of electron momentum. The dashed curve is a Monte Carlo shower prediction with .25 r.l. of aluminum upstream of the detector. The solid curve is the sum in quadrature of the shower calculation and 12 MeV of r.m.s. equivalent electronic noise. b) Resolution of module A extrapolated to zero material upstream of the counter. The error in the resolution at low energies is principally due to the

extrapolation to zero beam material. The curve is the sum in quadrature of the shower calculation (with no extra material) and the electronic noise. c) Resolution of module B extrapolated to zero material upstream of the counter. The curve is the sum in quadrature of the shower calculation (with no extra material) and the electronic noise.

6. Pulse height distributions in module A for a) 0.25, b) 1.0 and c) 4.0 GeV/c electrons.
7. Resolution (σ/E) vs. effective depth of the shower counter. Note that the resolution at lower energies can be improved by using only the first twelve radiation lengths, since the electronic noise contribution outweighs the signal at this depth in a low energy shower.
8. Deposition of collected shower energy in five sampling depths for 0.25, 1.0 and 4.0 GeV/c electrons.
9. Distribution of shower energy within the five sampling depths for a) 0.25 and b) 4 GeV/c electrons. The abscissa at each momentum is the fraction of the mean total energy observed. Thus, the 0.25 and 4 GeV/c scales differ by a factor of 16.
10. a) Collected charge as a function of electric field for 1 GeV/c electrons. b) Resolution (σ/E) in percent as a function of electric field for 1 GeV/c electrons. The curves are drawn to guide the eye.
11. a) Pulse height normalized to zero field vs. transverse magnetic field for 1 GeV/c electrons. b) R.m.s. deviation of the distribution of pulse height (normalized to zero field) vs. transverse magnetic field for 1 GeV/c electrons.

12. The r.m.s. deviations from the best fit straight line to the centroids of the charge deposition in different layers in depth for 1 GeV/c electron showers.
13. Distribution of the deviations from the best fit straight line in the first two radiation lengths for 1 GeV/c electrons.
14. Lateral shower spread in one dimension in each of the five depths for 1, 2 and 4 GeV/c electron showers.
15. Position uncertainty for 1 GeV/c electron showers as a function of strip width at different depths. The calculated curves are described in the text.
16. a) Total pulse height (Q_{tot}) in minions for 2 GeV/c electrons. b) Total pulse height (Q_{tot}) in minions for 2 GeV/c π^-.
17. Distribution of shower width vs. charge deposited in the first two radiation lengths for a) 4 GeV/c e^- and b) 4 GeV/c π^-.
18. Charge deposited in the first two radiation lengths vs. total charge for a) 1 GeV/c e^- and b) 1 GeV/c π^-. The distributions have been cut on the maximum width of the shower.
19. Charge deposited in the first four radiation lengths vs total charge for a) 1 GeV/C e^- and b) 1 GeV/c π^-. The distributions have been cut on the maximum width of the shower.
20. π^-/e^- rejection figures for 1,2 and 4 GeV/c particles with and without 1 r.l. of aluminum placed in front of the module. Curves are plotted for cuts on the charge in the first two r.l. ($Q_{1,2}$) vs. Q_{tot} with an additional cut on the shower width at the front of the device.

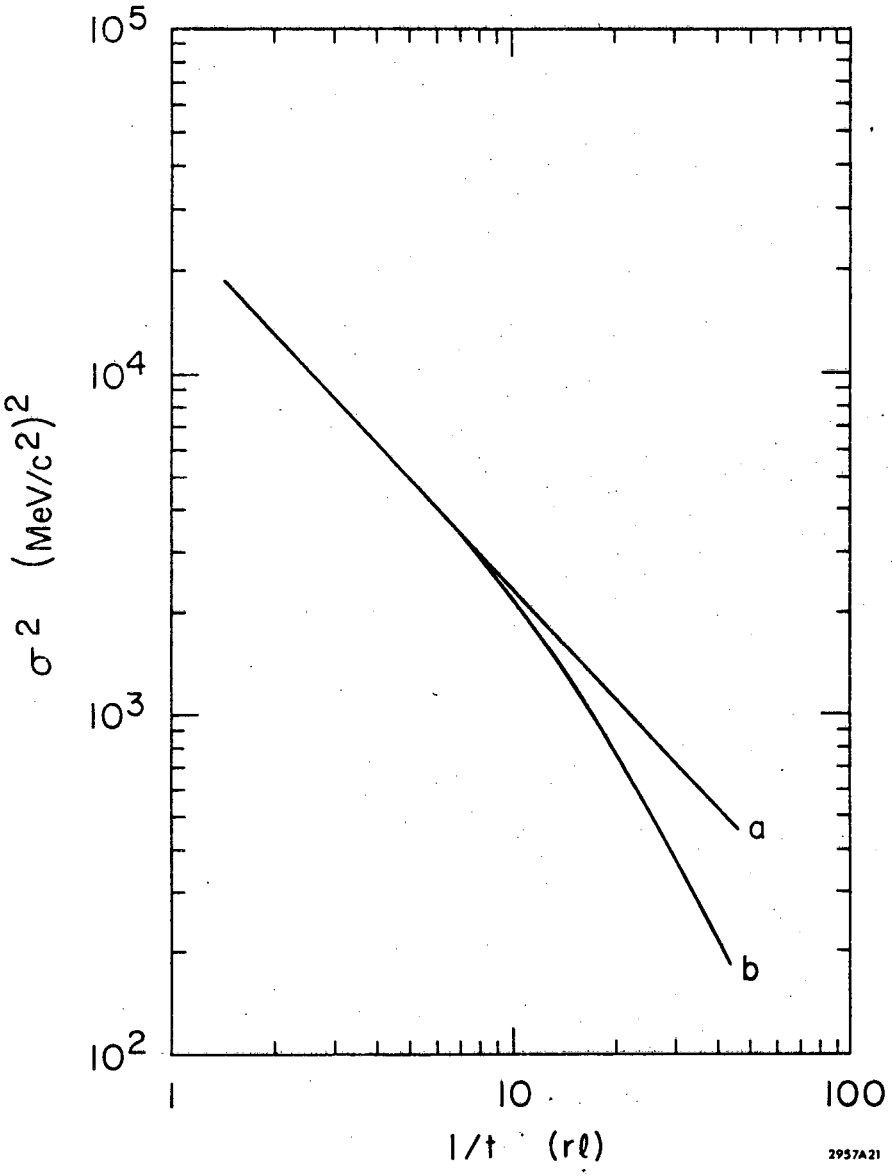
10^5
10^4
10^3
10^2
σ^2 (MeV/c2)^2
1
10
100
1/t (rℓ)
a
b
2957A21

Fig. 1

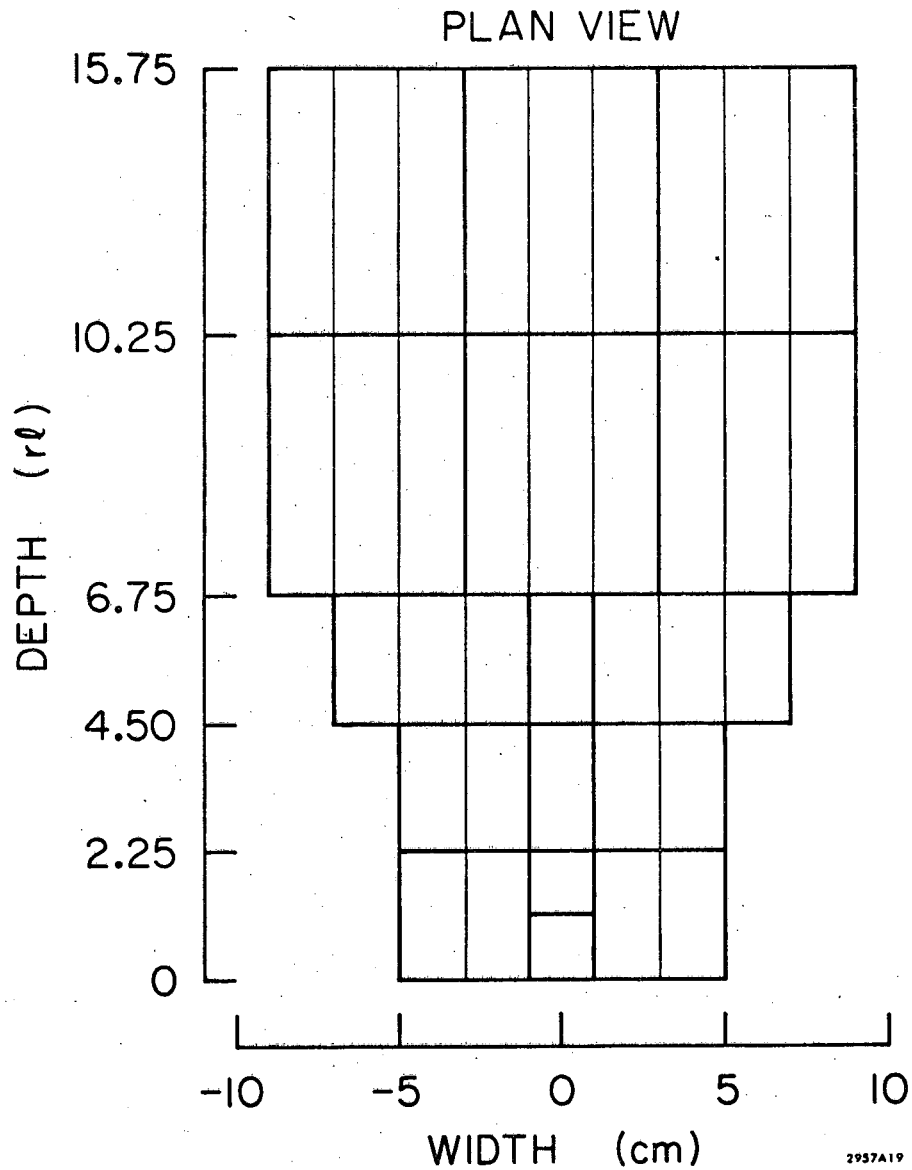
PLAN VIEW
15.75
10.25
6.75
4.50
2.25
0
DEPTH (rℓ)
-10
-5
0
5
10
WIDTH (cm)
2957A19

Fig. 2

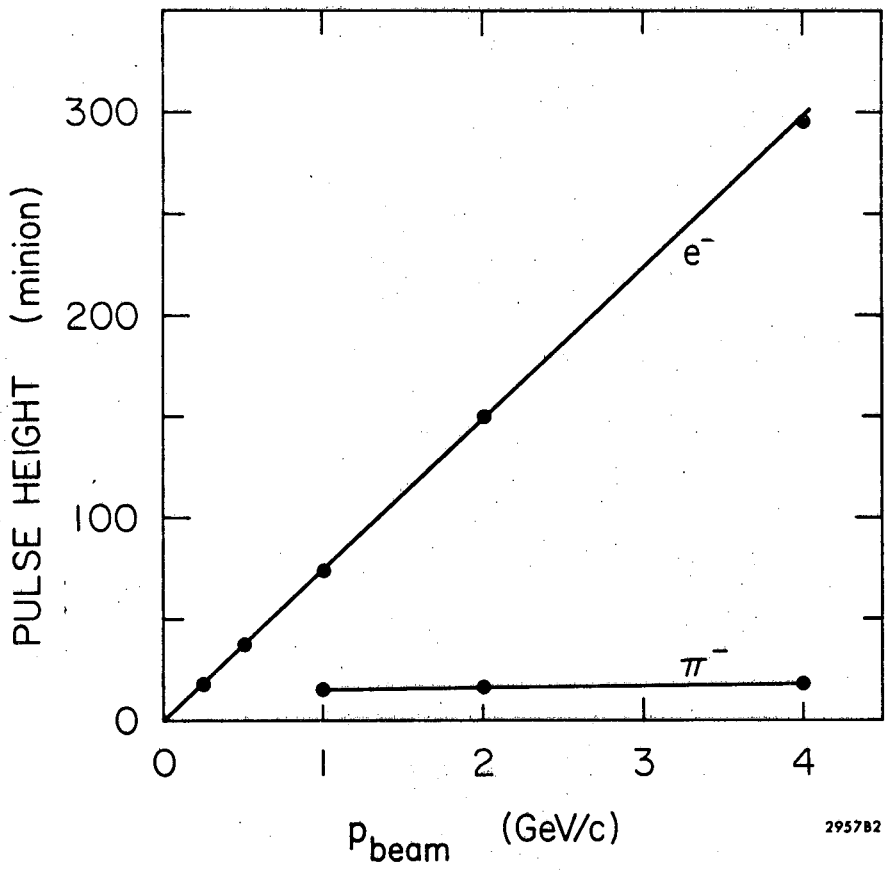
PULSE HEIGHT (minion)
300
200
100
0
0
1
2
3
4
e⁻
π⁻
p beam (GeV/c)
2957B2

Fig. 3

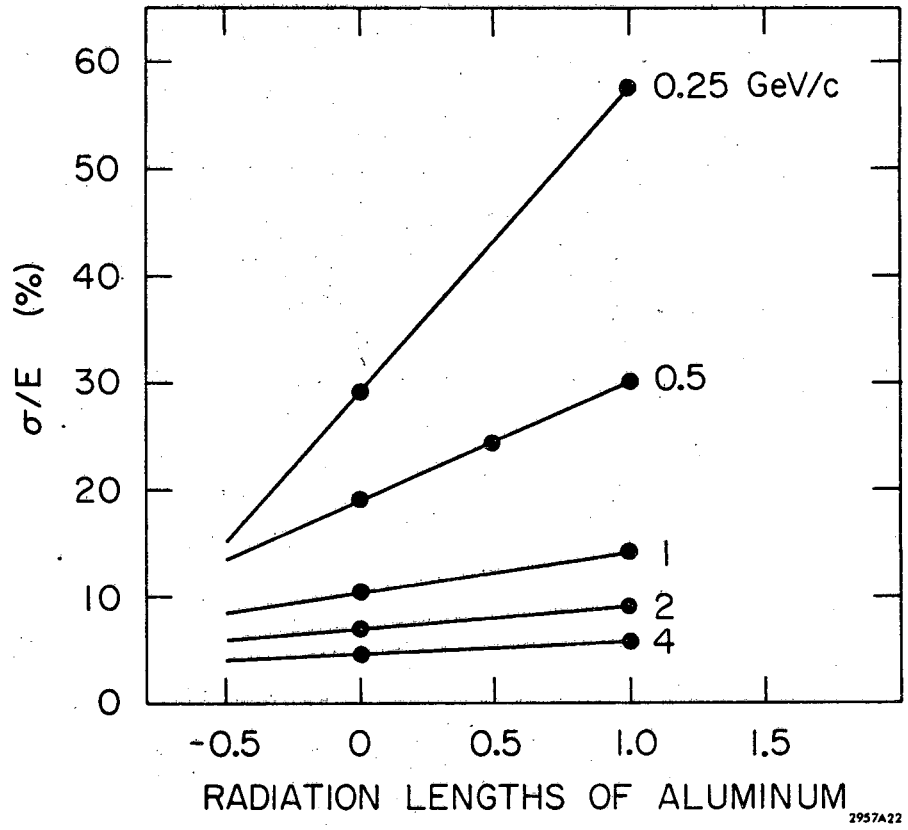
σ/E (%)
60
50
40
30
20
10
0
0.25 GeV/c
0.5
1
2
4
-0.5
0
0.5
1.0
1.5
RADIATION LENGTHS OF ALUMINUM
2957A22

Fig. 4

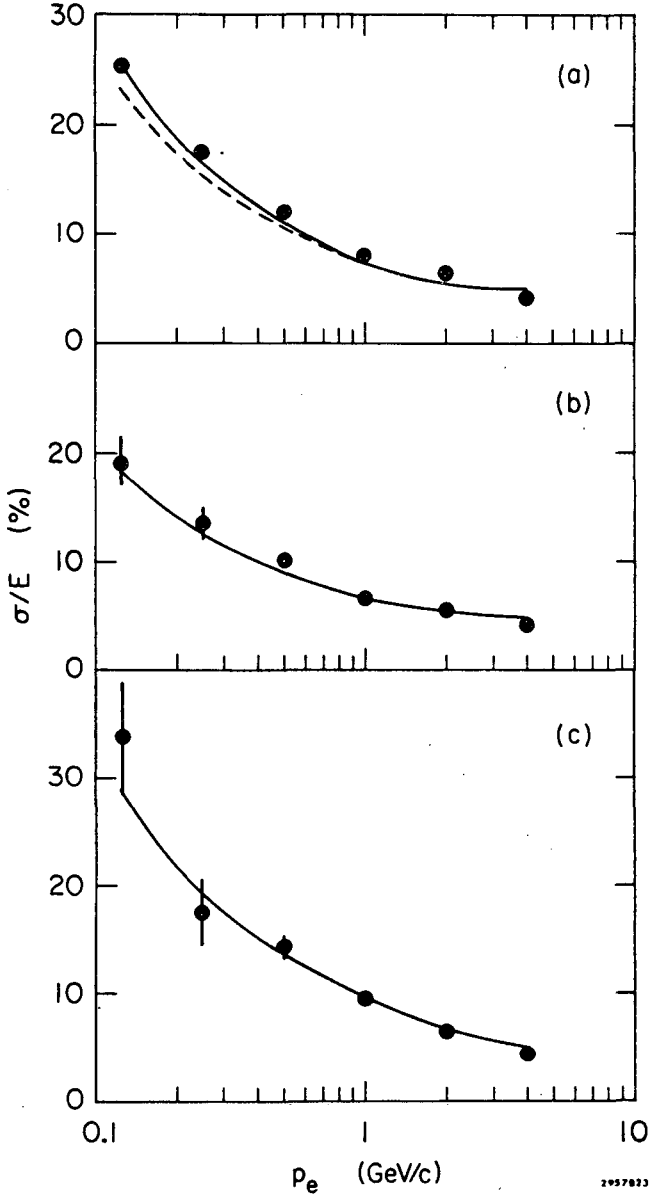
(a)
(b)
(c)
σ/E (%)
p_e (GeV/c)
0.1
1
10

Fig. 5

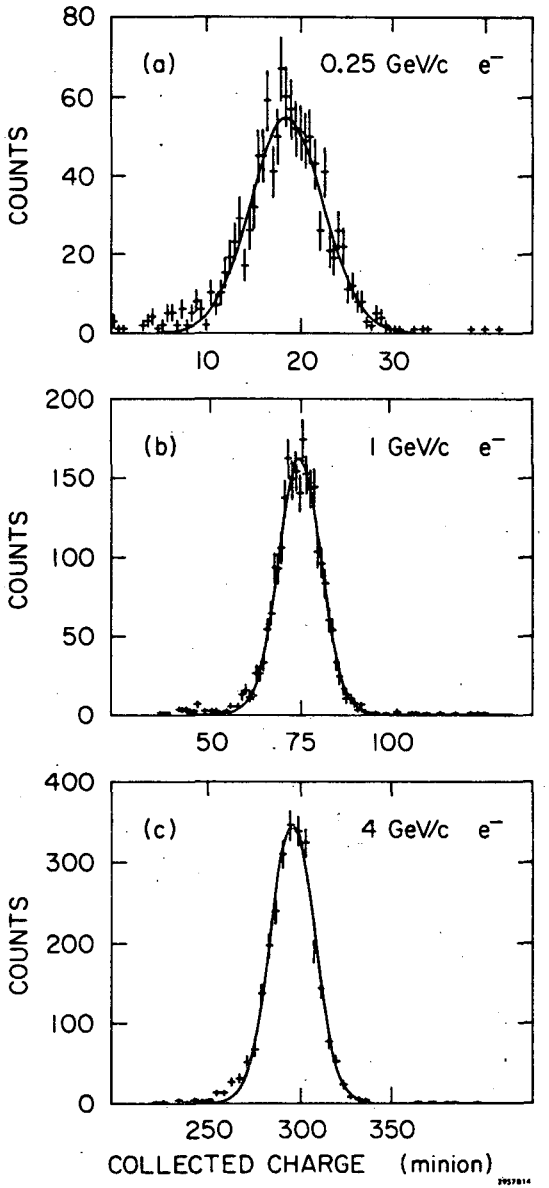
(a) 0.25 GeV/c e⁻
(b) 1 GeV/c e⁻
(c) 4 GeV/c e⁻
COUNTS
COLLECTED CHARGE (minion)

Fig. 6

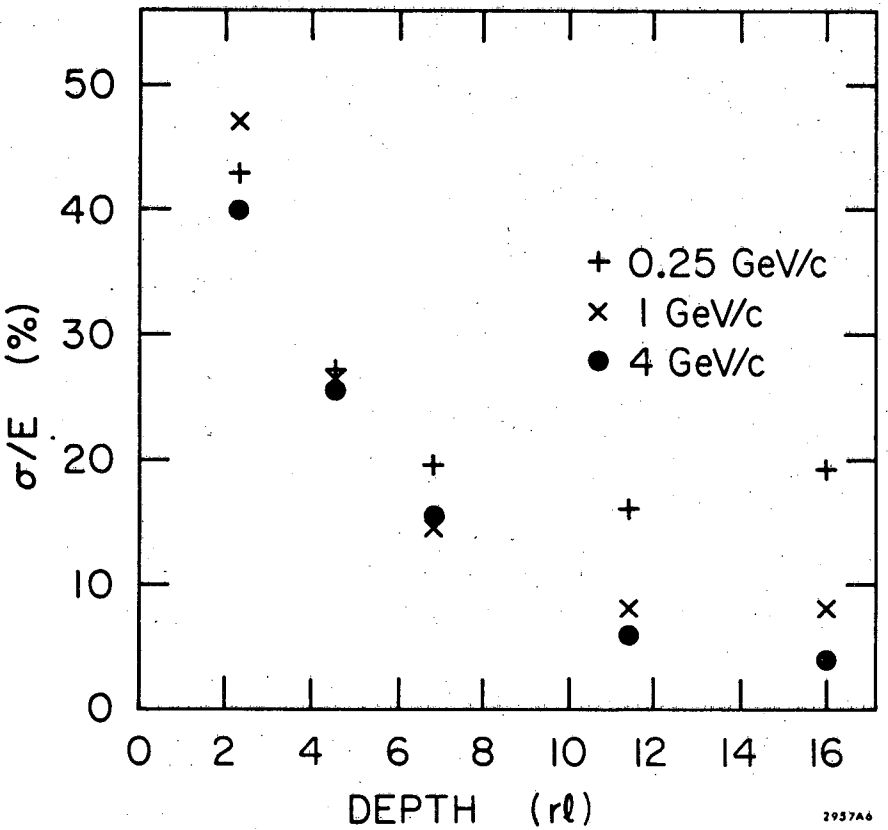
σ/E (%)
50
40
30
20
10
0
0 2 4 6 8 10 12 14 16
DEPTH (rℓ)
+ 0.25 GeV/c
× 1 GeV/c
● 4 GeV/c
2957A6

Fig. 7

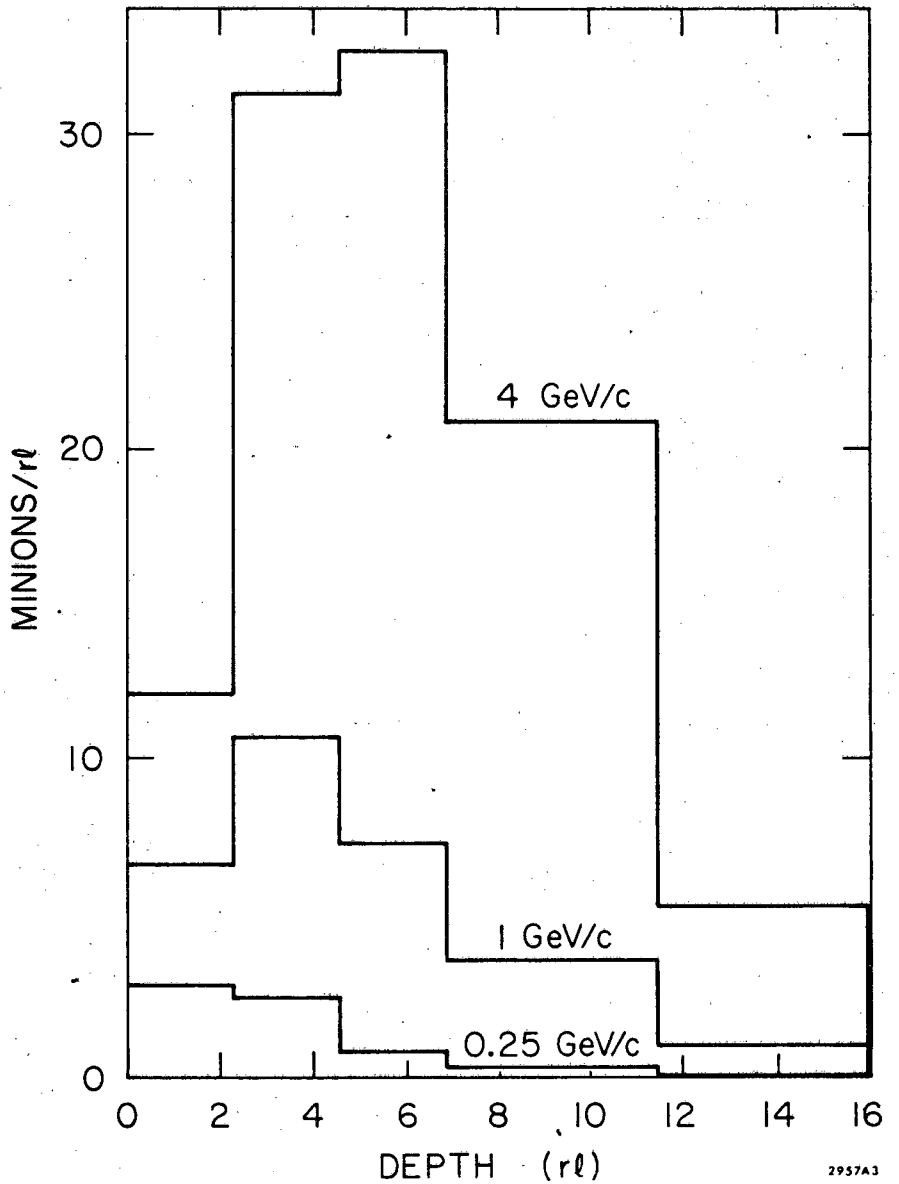
MINIONS/rℓ
30
20
10
0
0 2 4 6 8 10 12 14 16
DEPTH (rℓ)
4 GeV/c
1 GeV/c
0.25 GeV/c
2957A3

Fig. 8

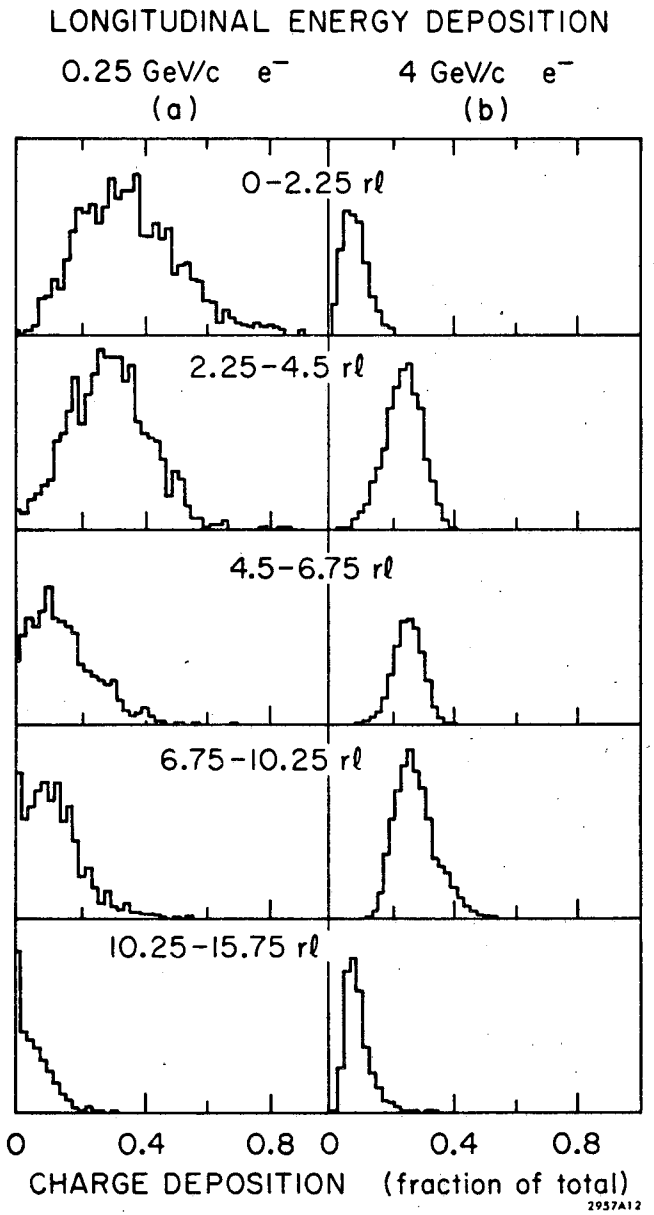
LONGITUDINAL ENERGY DEPOSITION
0.25 GeV/c e⁻
(a)
4 GeV/c e⁻
(b)
0-2.25 rℓ
2.25-4.5 rℓ
4.5-6.75 rℓ
6.75-10.25 rℓ
10.25-15.75 rℓ
0
0.4
0.8
0
0.4
0.8
CHARGE DEPOSITION (fraction of total)
2957A12

Fig. 9

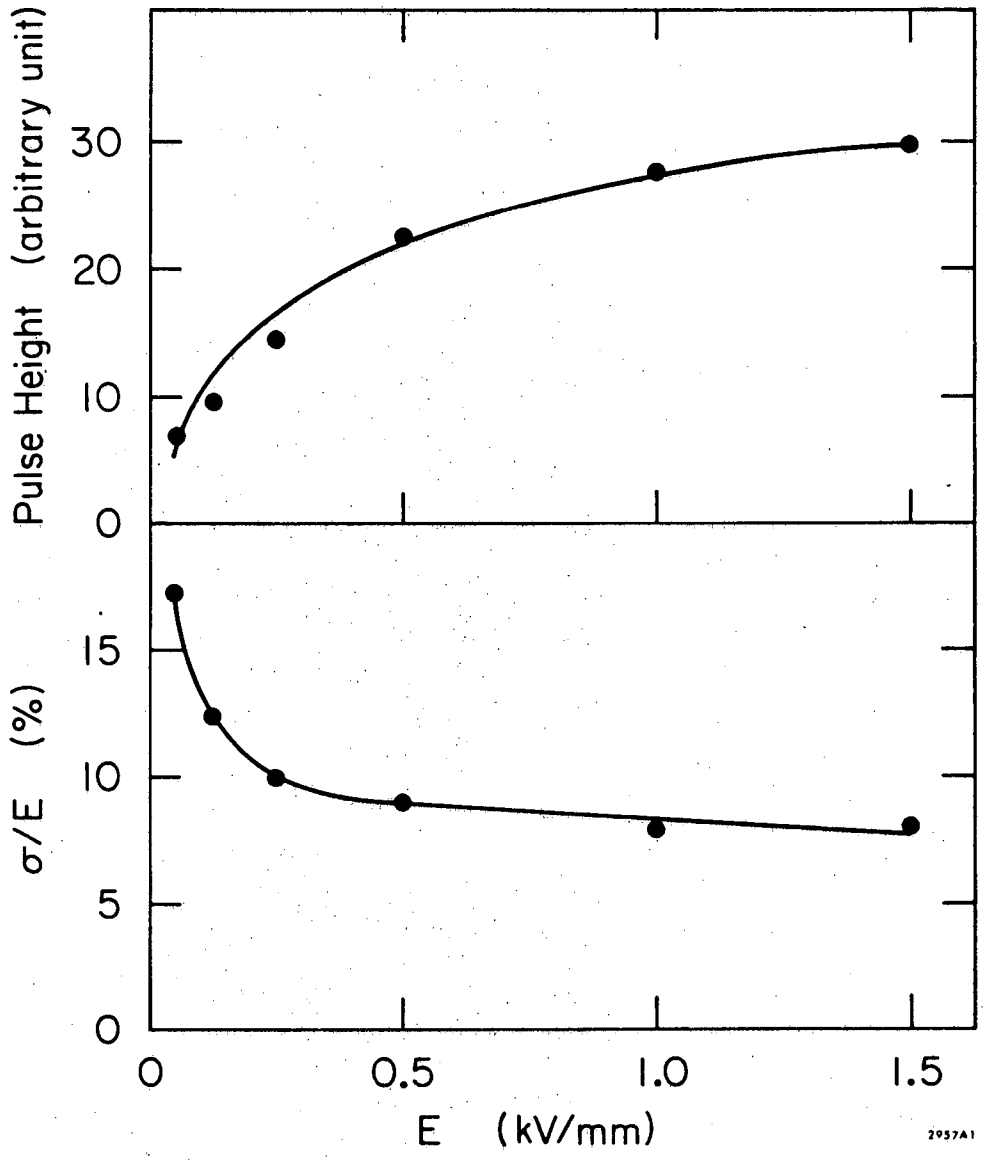
Pulse Height (arbitrary unit)
30
20
10
0
σ/E (%)
15
10
5
0
0
0.5
1.0
1.5
E (kV/mm)
2957A1

Fig. 10

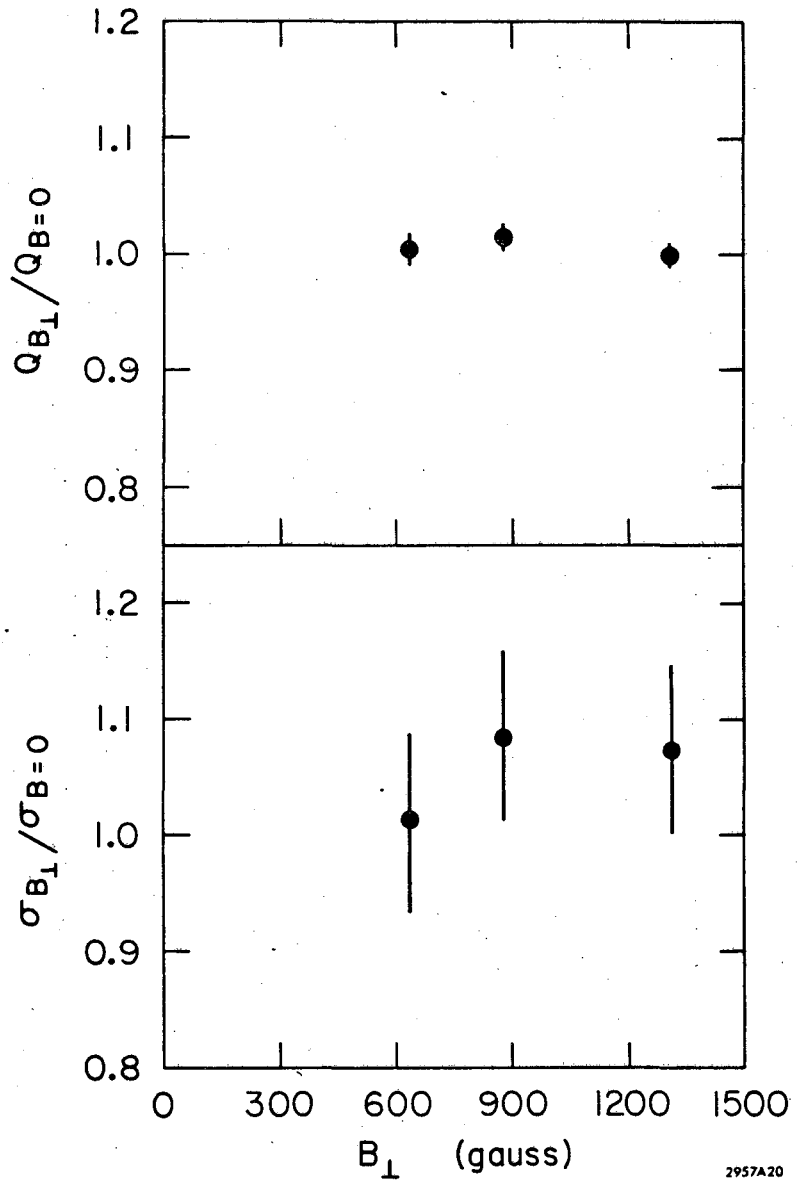
1.2
1.1
1.0
0.9
0.8
$Q_{B\perp}/Q_{B=0}$
1.2
1.1
1.0
0.9
0.8
$\sigma_{B\perp}/\sigma_{B=0}$
0
300
600
900
1200
1500
$B_\perp$ (gauss)
2957A20

Fig. 11

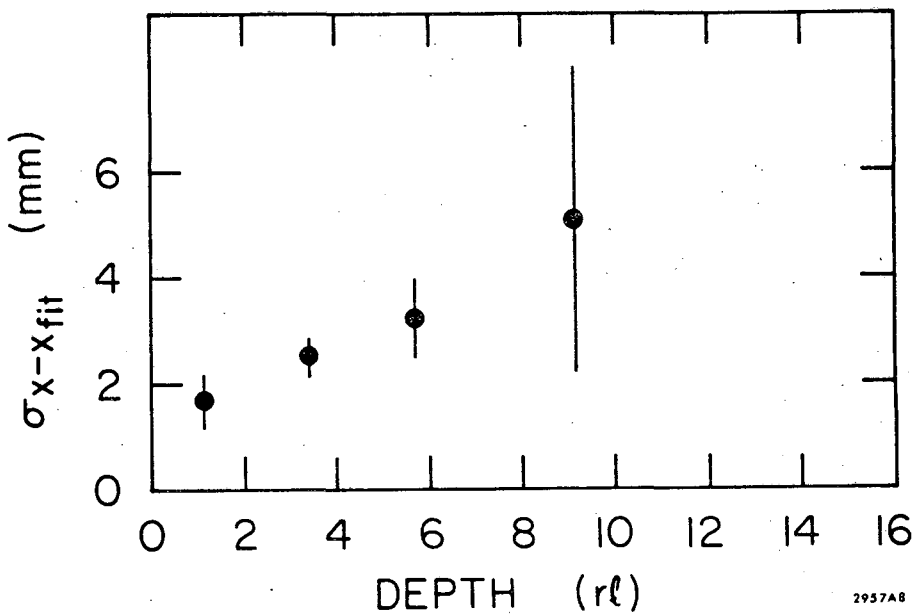
$\sigma_{x-x_{fit}}$ (mm)
0
2
4
6
0
2
4
6
8
10
12
14
16
DEPTH (rℓ)
2957A8

Fig. 12

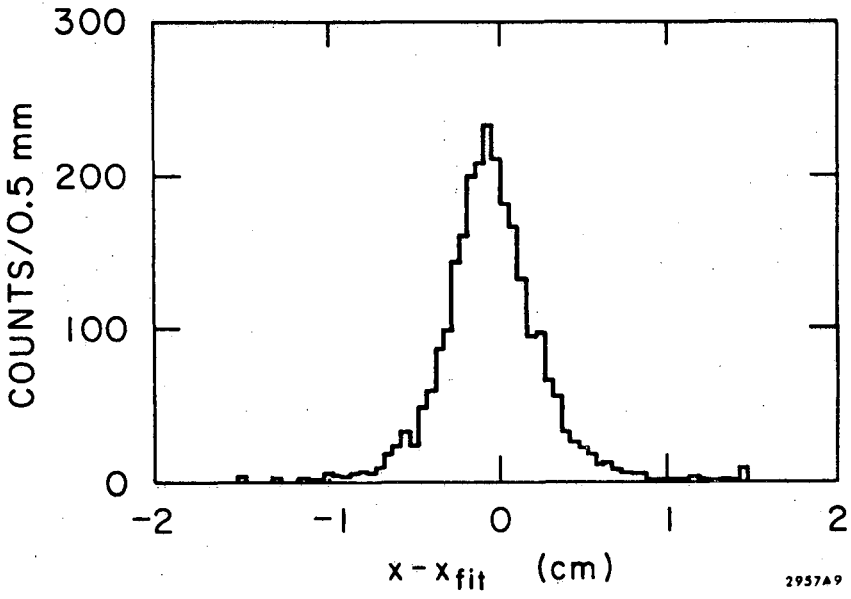
300
200
100
0
COUNTS/0.5 mm
-2
-1
0
1
2
x - x fit (cm)
2957A9

Fig. 13

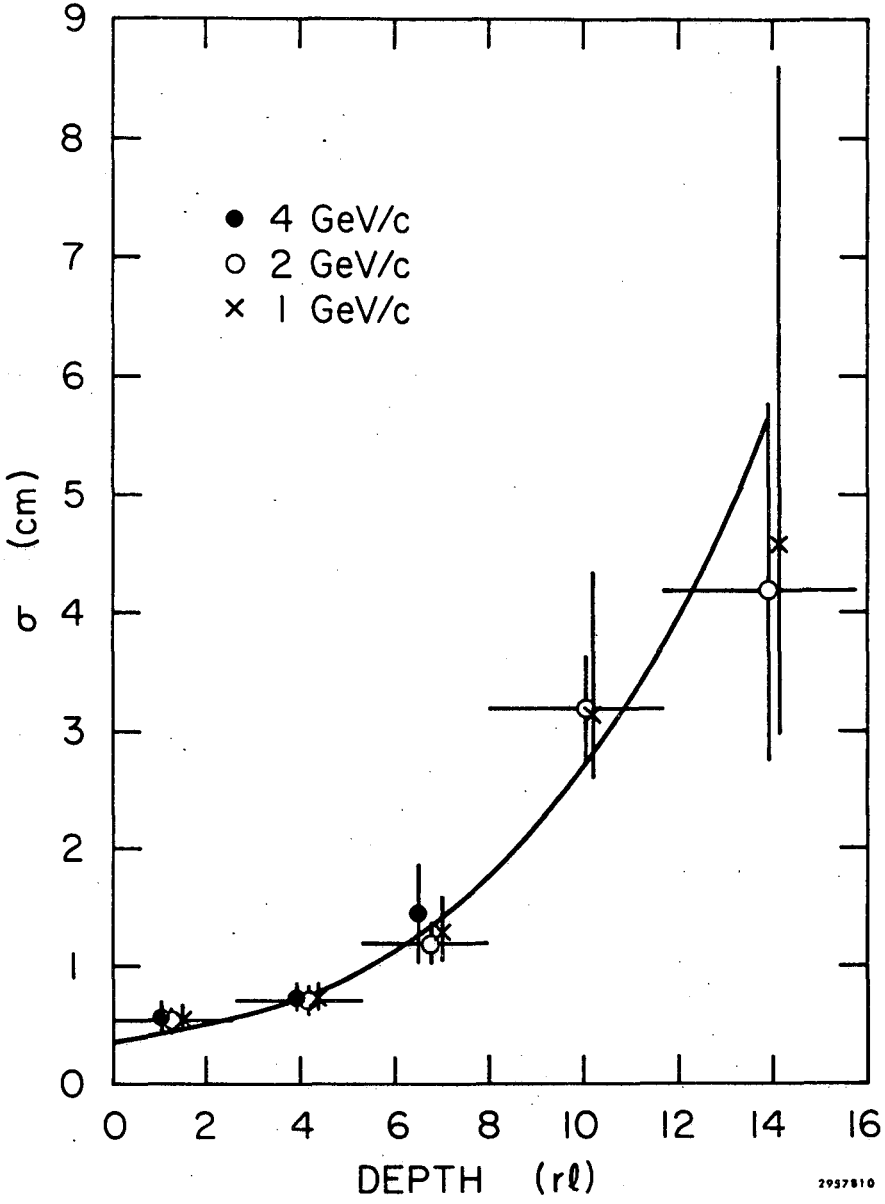
9
8
7
6
5
4
3
2
1
0
σ (cm)
4 GeV/c
2 GeV/c
1 GeV/c
0
2
4
6
8
10
12
14
16
DEPTH (rl)
2957B10

Fig. 14

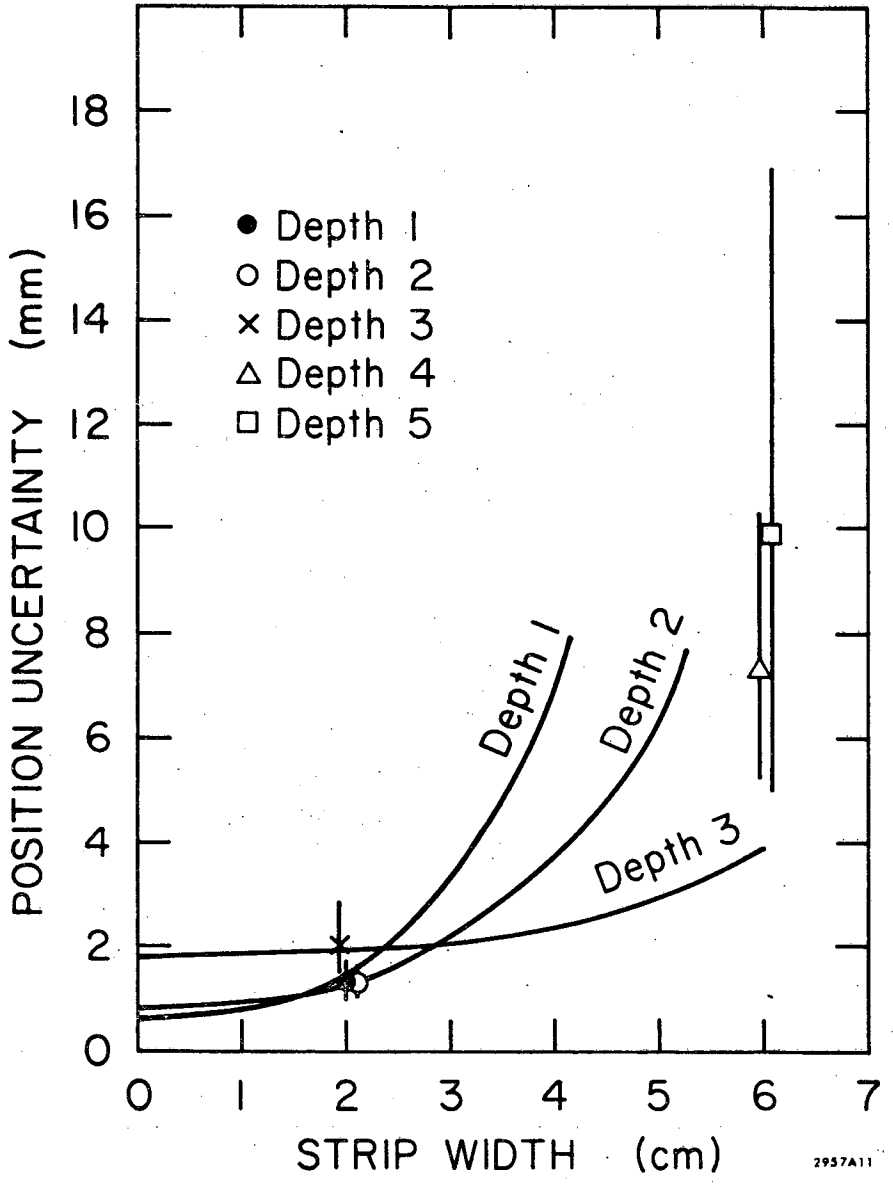
POSITION UNCERTAINTY (mm)
STRIP WIDTH (cm)
Depth 1
Depth 2
Depth 3
Depth 4
Depth 5
Depth 1
Depth 2
Depth 3
2957A11

Fig. 15

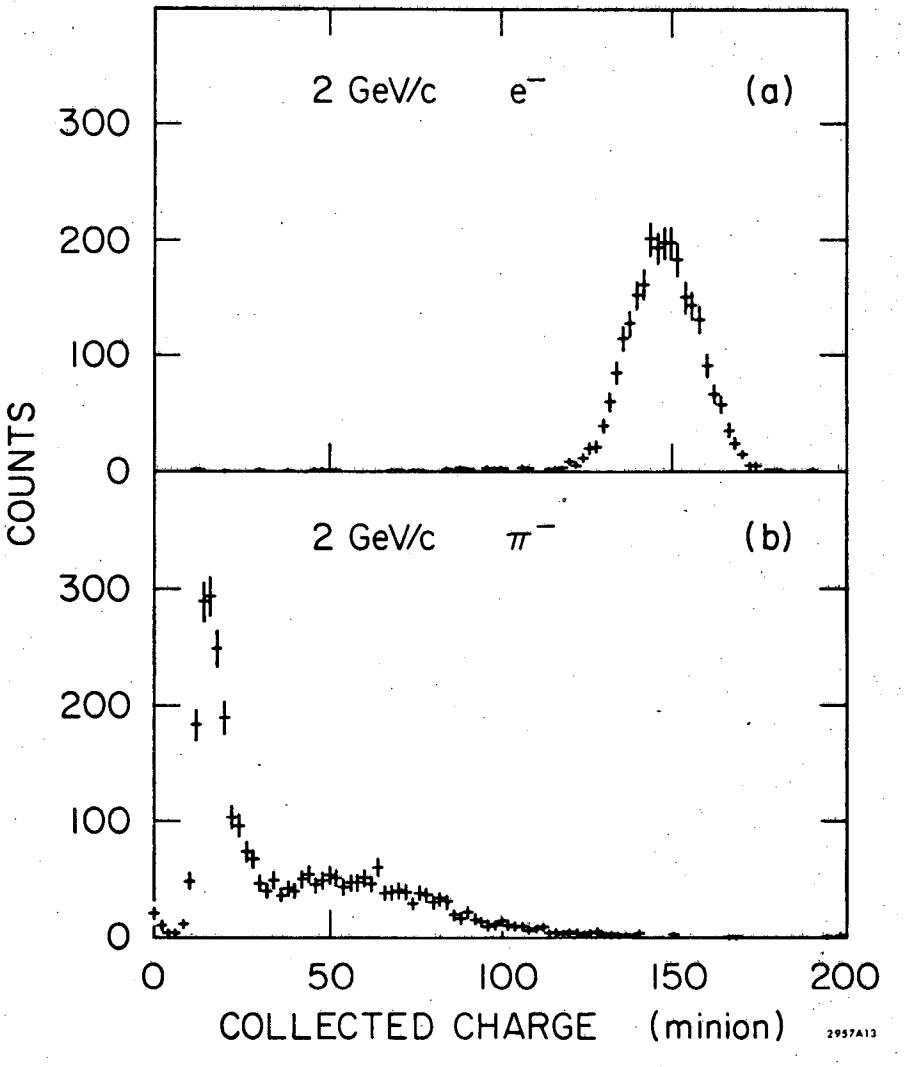
2 GeV/c e⁻
(a)
2 GeV/c π⁻
(b)
COUNTS
COLLECTED CHARGE (minion)
2957A13

Fig. 16

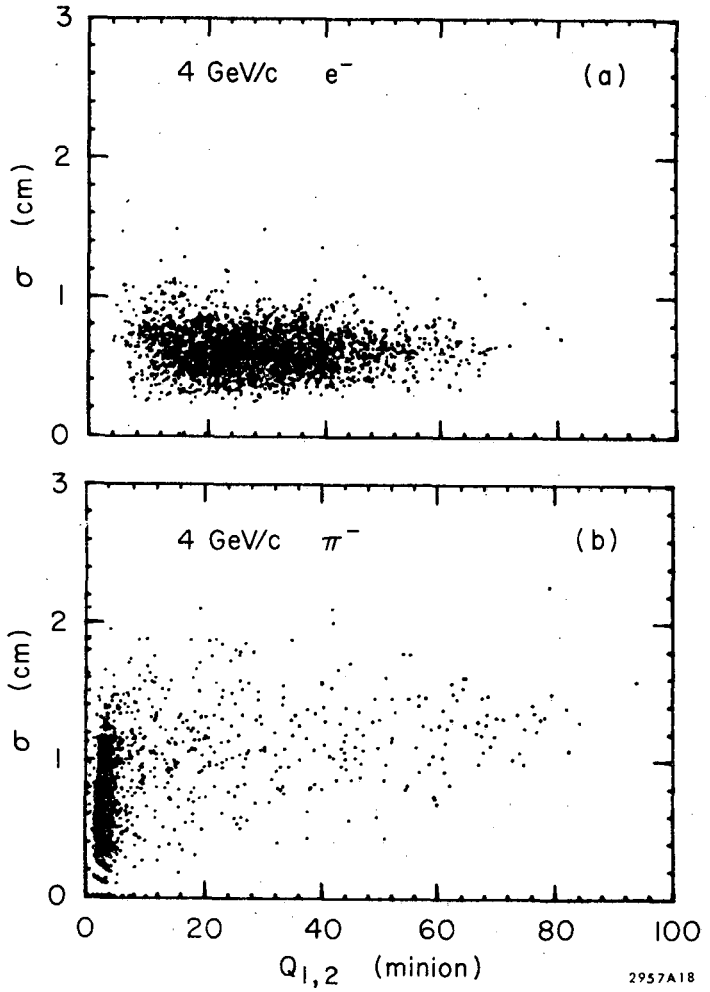
4 GeV/c e⁻
(a)
σ (cm)
4 GeV/c π⁻
(b)
σ (cm)
0
1
2
3
0
20
40
60
80
100
Q1,2 (minion)
2957A18

Fig. 17

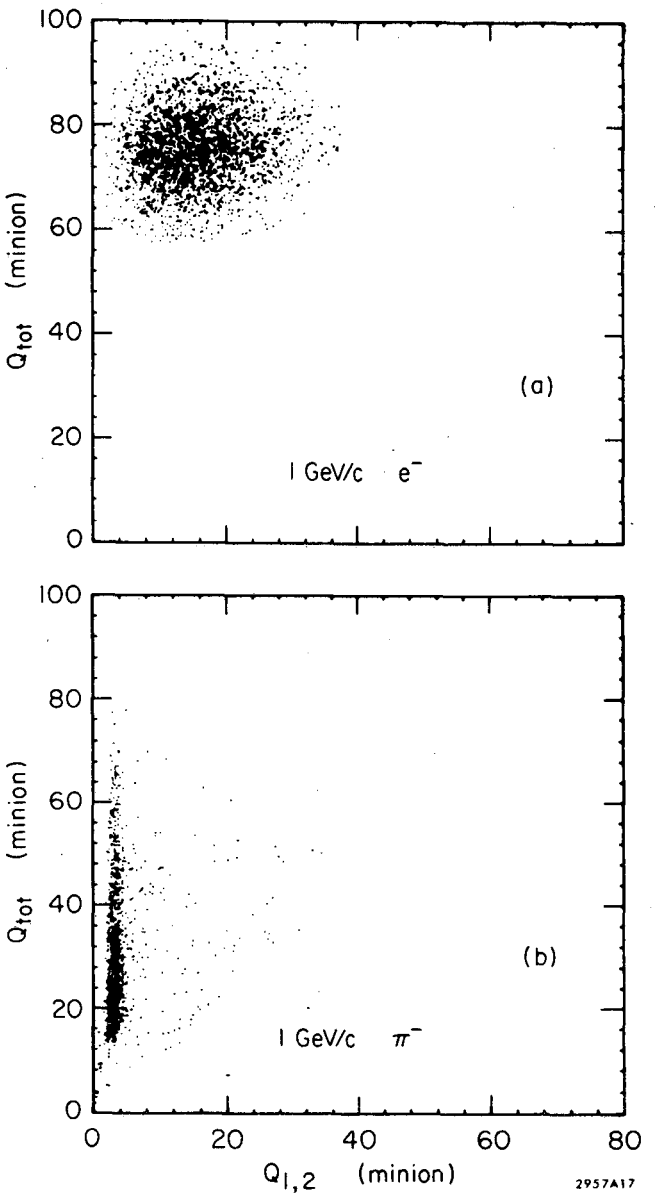
Qtot (minion)
(a)
1 GeV/c e⁻
Qtot (minion)
(b)
1 GeV/c π⁻
0
20
40
60
80
100
Q1,2 (minion)
2957A17

Fig. 18

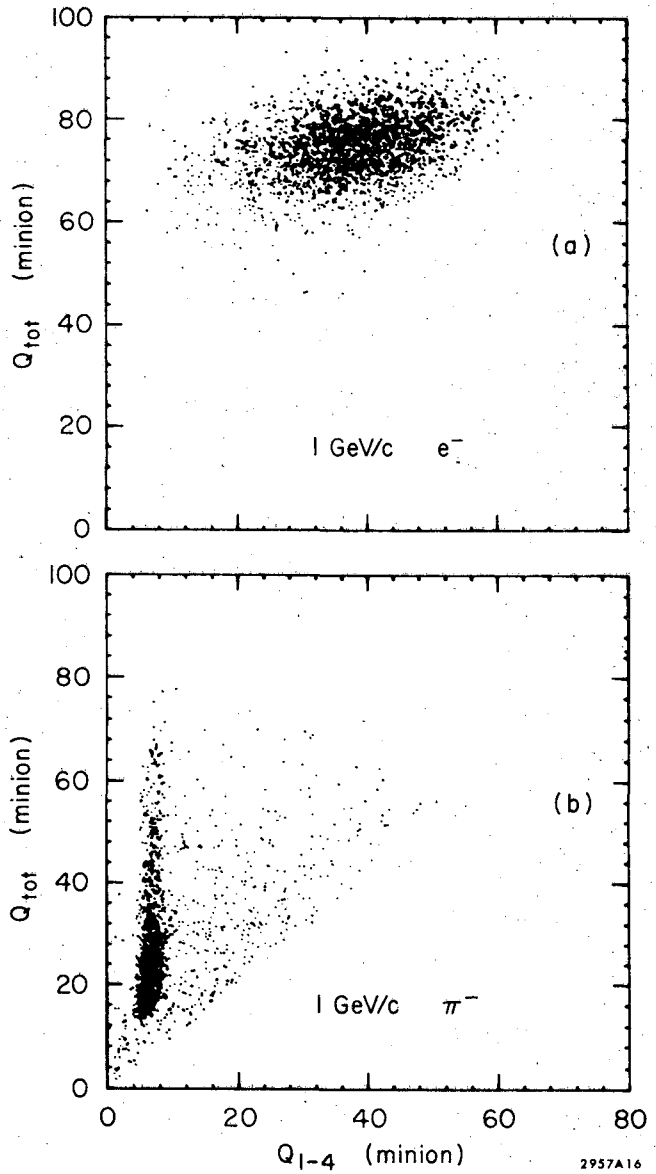
100
80
60
40
20
0
Q_{tot} (minion)
(a)
1 GeV/c e⁻
100
80
60
40
20
0
Q_{tot} (minion)
(b)
1 GeV/c π⁻
0
20
40
60
80
Q_{1-4} (minion)
2957A16

Fig. 19

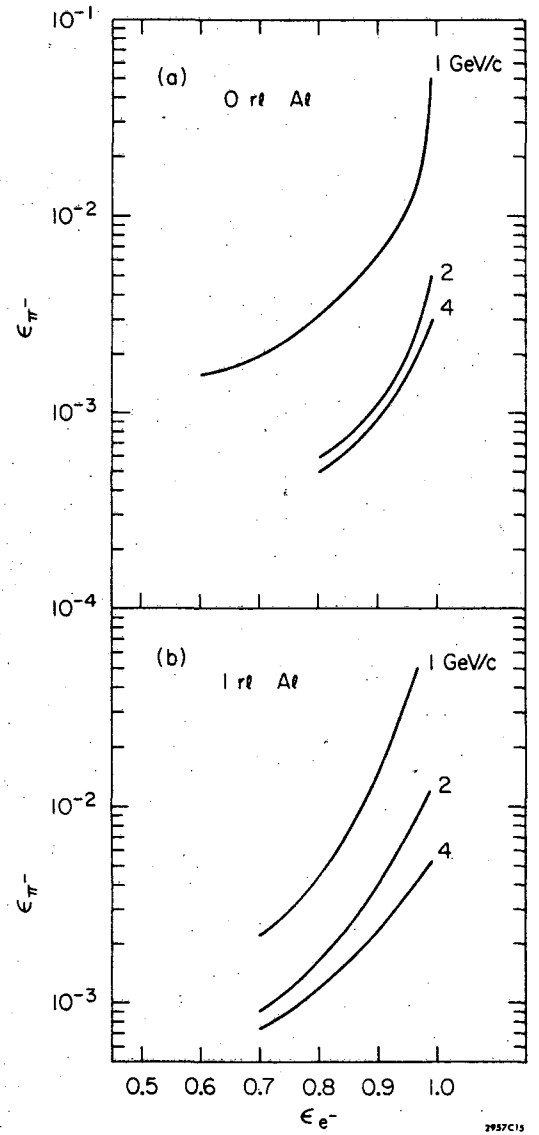
10^{-1}
10^{-2}
10^{-3}
10^{-4}
ϵ_{π^-}
(a)
O rℓ Aℓ
1 GeV/c
2
4
(b)
1 rℓ Aℓ
1 GeV/c
2
4
0.5
0.6
0.7
0.8
0.9
1.0
ϵ_{e^-}
2957C13

Fig. 20

TECHNICAL INFORMATION DIVISION
LAWRENCE BERKELEY LABORATORY
UNIVERSITY OF CALIFORNIA
BERKELEY, CALIFORNIA 94720